Journal of Structural Geology 140 (2020) 104132

Contents lists available at ScienceDirect

Journal of Structural Geology

journal homepage: http://www.elsevier.com/locate/jsg

Shear localisation, strain partitioning and frictional melting in a debris avalanche generated by volcanic flank collapse

Amy Hughes [a,*], Jackie E. Kendrick [a], Guido Salas [b], Paul A. Wallace [a], François Legros [c], Giulio Di Toro [d], Yan Lavallée [a]

[a] Department of Earth, Ocean and Ecological Sciences, University of Liverpool, Liverpool, L69 3GP, United Kingdom
[b] Department of Geology and Geophysical Sciences, National University of San Agustin, Arequipa, Peru
[c] Freelance researcher, Arequipa, Peru
[d] Department of Geoscience, University of Padova, Via Gradenigo, 6, 35131, Padova, Italy

ARTICLE INFO

Keywords:
Sector collapse
Pseudotachylyte
Strain partitioning
Shear localisation
Cataclasis

ABSTRACT

The Arequipa volcanic landslide deposit to the east of Arequipa (Peru) originated from the Pichu Pichu volcanic complex, covering an area ~200 km^2. The debris avalanche deposit exhibits internal flow structures and basal pseudotachylytes. We present field, microstructural and chemical observations from slip surfaces below and within the deposit which show varying degrees of strain localisation. At one locality the basal shear zone is localised to a 1–2 cm thick, extremely sheared layer of mixed ultracataclasite and pseudotachylyte containing fragments of earlier frictional melts. Rheological modelling indicates brittle fragmentation of the melt may have occurred due to high strain rates, at velocities of >31 m s^{-1} and that frictional melting is unlikely to provide a mechanism for basal lubrication. Elsewhere, we observe a ~40 cm thick basal shear zone, overprinted by sub-parallel faults that truncate topological asperities to localise strain. We also observe shear zones within the avalanche deposit, suggesting that strain was partitioned. In conclusion, we find that deformation mechanisms fluctuated between cataclasis and frictional melting during emplacement of the volcanic debris avalanche; exhibiting strain partitioning and variable shear localisation, which, along with underlying topography, changed the resistance to flow and impacted runout distance.

1. Introduction

Volcanic edifices are inherently unstable structures formed by the superimposition of layers of varying volcanic materials on relatively rapid geological timescales (Voight, 2000; Acocella and Puglisi, 2010). Structural instability of volcanoes and other orogenic landforms can be prompted by a range of factors such as: magma intrusion (e.g., Mount St. Helens; Lipman and Mullineaux, 1981); overloading of flanks (Swanson et al., 1976), tectonic stresses (Lagmay et al., 2000), ground motion during earthquakes (Voight and Elsworth, 1997), hydrothermal activity (Day, 1996; Voight and Elsworth, 1997), alteration (Reid, 2004), precipitation (McGuire, 1996), freeze-thaw (Kawamura and Miura, 2013), and erosion (McGuire, 1996). This is combined with a natural variability in coherency, porosity, crystallinity and glass content of materials, which affects the strength and primary deformation mode (e.g., brittle vs ductile) of the edifice-forming rocks (e.g. Heap et al., 2010; Benson et al., 2012). Collapses of unstable volcanic structures occur at a wide range of scales, the smallest examples form from shallow slope instability events (Cecchi et al., 2004) and rockfalls (Calder et al., 2002), whereas larger scale instabilities can produce deep-seated slip events that may subject magmatic systems to decompression that triggers unrest and even eruptions (e.g. Hunt et al., 2018).

Large-scale collapse landslides pose significant hazards to life and property within the spatial range of the event (e.g. Siebert, 1992). Quantifying the potential distance these collapses may travel, the rate at which onset occurs and the speed of the avalanche itself as it propagates from the source area is therefore paramount in hazard risk assessments. Large landslide volumes can exceed 10^9 m^3 (Siebert, 1984) and travel at speeds up to 100 m s^{-1} (Siebert et al., 1987; Shea and van Wyk de Vries, 2008) and those with volumes in excess of 10^6 m^3 often exhibit anomalously high mobility (Scheidegger, 1973). Mobility considers a combination of velocity and runout distance from source (Iverson et al., 2015), which can often be greater than ten times the height of fall (the elevation change from source to final position of the mass of material) in

* Corresponding author.
E-mail address: amy.hughes@liverpool.ac.uk (A. Hughes).

https://doi.org/10.1016/j.jsg.2020.104132
Received 24 December 2019; Received in revised form 26 June 2020; Accepted 30 June 2020
Available online 3 July 2020

these instances (Legros, 2002). Analysis of the ratio of height of fall to runout distance against volume of landslides highlights that landslides with larger volumes travel longer distances, suggesting the importance of a mechanism that acts to lower frictional coefficients, allowing them to be more mobile than predicted by simple frictional sliding models (Shea and van Wyk de Vries, 2008). Such behaviour has been identified in events developing in all rock types (Legros, 2002 and references therein), suggesting a commonality of the process. Several mechanisms to reduce frictional coefficients during frictional sliding of landslides have been put forth, including: mechanical fluidisation (Davies, 1982; Campbell et al., 1995), the lubricating effects of basal groundwater or ice (Lucchitta, 1987; Legros, 2002; De Blasio, 2011), trapped air (Shreve, 1968), salt (De Blasio, 2011), acoustic fluidisation (Melosh, 1979, 1986; Johnson et al., 2016), mechanical and thermal fluid pressurisation (e.g. Ferri et al., 2011) elastohydrodynamic lubrication (Brodsky and Kanamori, 2001), frictional velocity weakening (e.g. Wang et al., 2017) and the formation of a lubricating frictional melt layer (Legros et al., 2000; De Blasio and Elverhøi, 2008; Wang et al., 2017).

The production of frictional melts is the result of frictional heating due to strain localisation onto a discrete, thin slipping layer (Sibson, 1975). These frictional melts are then preserved in the geological record as pseudotachylytes, often resulting from seismogenic fault activity (Sibson, 1975, 1977; Spray, 1992; Shimamoto and Lin, 1994; Di Toro et al., 2006; Nielsen et al., 2008), shear localisation in volcanic conduits (e.g. Kendrick et al., 2012), and at the basal contacts of some mass movements (Erismann, 1979; Masch et al., 1985; Legros et al., 2000; Lin et al., 2001; Hacker et al., 2014; Bernard and van Wyk de Vries, 2017). The presence of frictional melts along fault slip zones has often been suggested to act as a lubricant (Di Toro et al., 2006); yet, they may conversely act as a viscous brake (Fialko and Khazan, 2005), especially in intermediate and felsic volcanic rocks sheared at low (<10 MPa) normal stresses or low lithostatic loads (Lavallée et al., 2012; Kendrick et al., 2014; Hornby et al., 2015). Importantly, the transient physico-chemical evolution of frictional melt during slip impacts rheological evolution (Lin and Shimamoto, 1998; Wallace et al., 2019), which controls slip velocity, shear resistance and any thermo-mechanical feedback due to viscous energy dissipation (Nielsen et al., 2010) that, in the case of mass movements, may ultimately regulate the runout distance.

Careful examination of the internal structures of mass movement deposits, such as large landslides (including debris avalanches), suggests a spectrum of behaviour; from those which disaggregate during transport to those transported over long distances whilst maintaining their coherence, exhibited by undisturbed structures such as discrete lithological units and intrusions (Glicken, 1998; Erismann and Abele, 2001; Hacker et al., 2014). Some evidence suggests that larger events have preserved their internal structures (Erismann and Abele, 2001; De Blasio and Elverhøi, 2008). In order to preserve these features, shear must have been localised to a relatively narrow layer to prevent wholescale deformation. Shear localisation is an integral part of flow segregation and means that the basal mechanisms of debris avalanches and volcanic collapses largely control emplacement. On this layer, shear rates (and thus frictional heating) may be extremely high as a result of the high velocity of the mass movement (De Blasio and Elverhøi, 2008). Pseudotachylytes have only been identified at the base of a few landslides, including: Kofels, Austria (Erismann, 1979); Langtang, Nepal (Masch et al., 1985); Tsaoling, Taiwan (Lin et al., 2001); Markagunt slide, Utah (Hacker et al., 2014), Sevier slide, Utah (Biek et al., 2019), French Massif Central (Bernard and van Wyk de Vries, 2017) and Arequipa, Peru (Legros et al., 2000). The Arequipa volcanic landslide deposit displays a rare example of preserved pseudotachylyte at the base of a landslide originating from a volcanic source, namely Pichu Pichu volcano. The internal structure of the deposit is exposed owing to multiple incisions by rivers since emplacement >1 Ma ago (Legros et al., 2000). Here we present new observations from an extensive geological survey of the Arequipa volcanic landslide deposit, including re-examination of the original outcrops investigated in Legros et al. (2000) as well as newly identified shear exposures.

2. Geological background

Pichu Pichu is part of the modern Central Andean Volcanic Zone and is located along the NE margin of the Arequipa basin, 30 km to the east of the city of Arequipa (Fig. 1). The volcanic arc trends approximately NW-SE, associated with major regional sinistral strike-slip faults trending NW-SE (de Silva and Francis, 1990; Lavallée et al., 2009). The Arequipa basin is filled with four distinct, high-K calc-alkaline ignimbrites commonly referred to as the "Sillar" (Lebti et al., 2006). These range in age from the 13.19 ± 0.09 Ma Rio Chili Ignimbrite to the 1.03 ± 0.09 Ma Yura Tuff (Lebti et al., 2006). The source of these ignimbrites has been inferred to evidence a relict volcanic caldera now buried by the construction of Chachani volcanic complex during the quaternary (in the last 1 Ma to 642 ka; Aguilar Contreras et al., 2016). Similarly, the ignimbrites underlie the younger Arequipa volcanic landslide deposit (Legros et al., 2000; Lebti et al., 2006) estimated to have occurred at ~1 Ma (Lebti et al., 2006).

Pichu Pichu itself is an extinct volcanic complex with andesitic lava flows dated to 6.71 ± 0.57 Ma using K-Ar dating (Kaneoka and Guevara, 1984) with no evidence of younger activity. The collapse of a significant portion of the volcanic flank resulted in the formation of an open arcuate ridge morphology, facing the large volcanic debris avalanche deposit found to the east of Arequipa (Fig. 1). Initially the deposit was mapped to extend to the NE of Arequipa, however further investigation of those deposits found that the chemistry of entrained lava blocks and flow package characteristics more closely correlate to lava flows from an earlier cone of El Misti that underwent collapse before the formation of the modern day cone (Thouret et al., 2001). These more recent flows partially overlie and obscure the older collapse deposits now interpreted to originate from Pichu Pichu. More recently the northern boundary of the debris flow deposit was re-mapped in the area of Chiguata to follow the break in slope between the flank of El Misti and the irregular topography identified as the Pichu Pichu collapse formation (Thouret et al., 2001). The debris avalanche deposit has been stated to evidence both mixed and block facies using nomenclature of Glicken (1991), and has a basal pseudotachylyte (Legros et al., 2000), but has not been mapped in detail (Thouret et al., 2001).

3. Methods

The debris avalanche deposit was surveyed in 2017. Topographic maps were used to identify valleys and gullies that would be potential sites for basal exposures using the relative altitudes from the previously identified basal contact (Legros et al., 2000) at 2600 m above sea level. Where basal contacts were located, we also examined the debris avalanche deposit above for internal flow features.

Samples were collected from several localities; for basal contacts samples were generally taken from above, below and within the shear zone. For all samples, flow direction was noted (determined from the position from source, clast imbrication and striations if present) in the field and ascribed to each specimen to enable structural analysis. Orientated, polished thin sections were used for both microtextural and geochemical analyses. Backscattered electron images (BSE) used for microtextural analysis were taken on a Phillips XL30 scanning electron microscope (SEM) at the University of Liverpool with 20 kV accelerating voltage and 10 μm working distance.

Bulk chemistry was determined by X-ray fluorescence (XRF) at the University of Leicester using a PANalytical Axios Advanced XRF Spectrometer. Major element analyses were determined from glass beads fused from ignited powders and trace elements on pressed powder pellets. Relative precision and accuracy were better than 1.5% for major elements and 5% for trace elements based on a series of repeat analyses on reference materials (Bardon Hill granodiorite and Whin Sill dolerite;

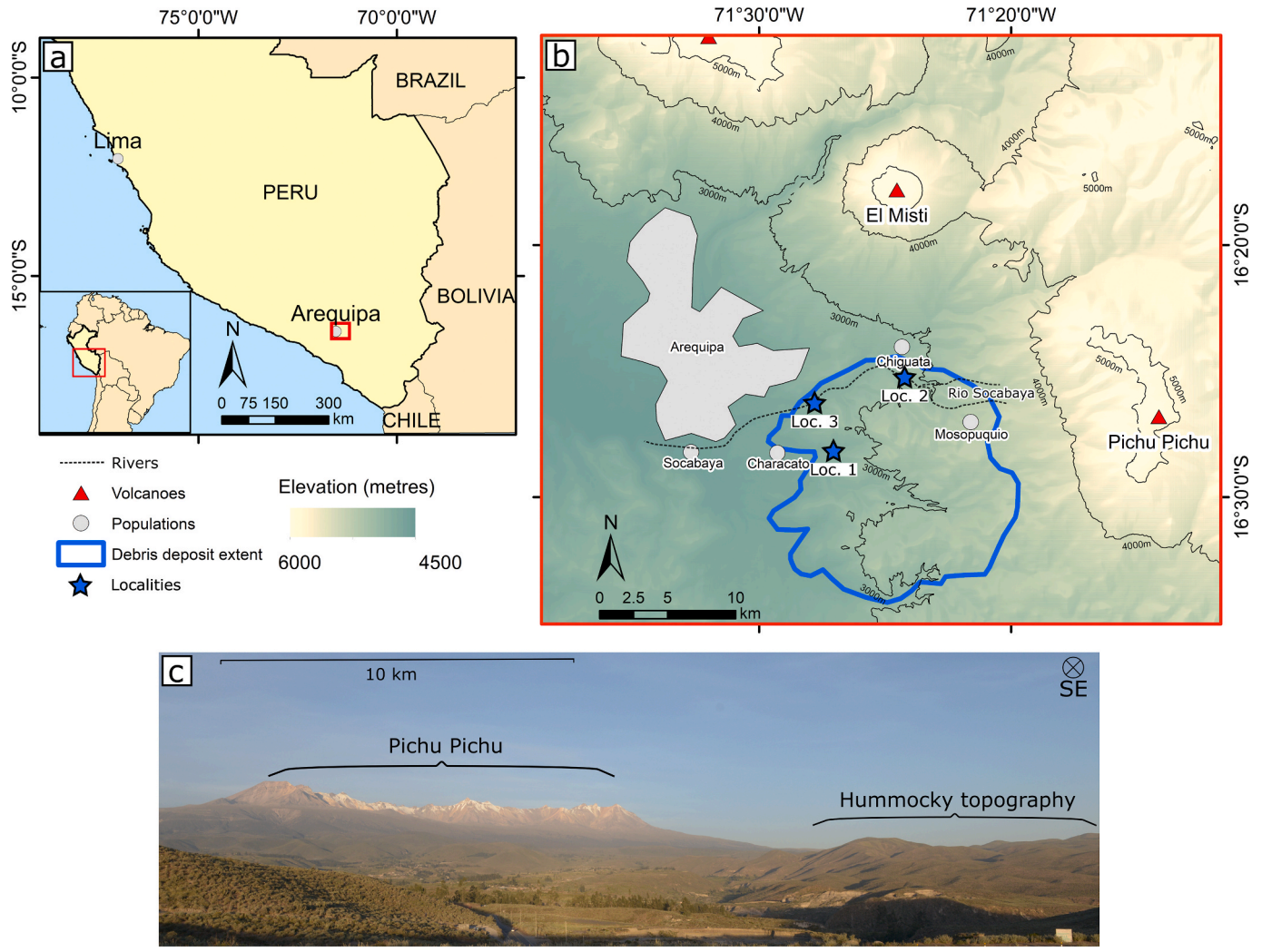

Fig. 1. Locality map and field photos to illustrate debris avalanche deposit and source location. a) Map of southern Peru (red box marks area in b) with inset of South America (red box shows the map area). b) Topographic map of the Arequipa basin, Pichu Pichu, the debris avalanche deposit (blue outline) and field localities for this study (Loc. 1–3). c) Photo of dissected Pichu Pichu arcuate ridge and the debris avalanche deposit showing raised humocky topography, view is SE from Chiguata. (For interpretation of the references to colour in this figure legend, the reader is referred to the Web version of this article.)

see supplementary materials).

The geochemical compositions of phases in the underlying ignimbrite, pseudotachylytes, cataclasites and lithic clasts from within the debris avalanche were measured using a Cameca SX100 electron probe micro-analyser (EPMA) at the University of Manchester, using wavelength dispersive spectroscopy (WDS). Calibration of the detectors were conducted on a range of standards (albite for Si and Na, wollastonite for Ca, fayalite for Fe, corundum for Al, ilmenite for Ti, periclase for Mg, tephrite for Mn and potassium feldspar for K). These standards were revisited at the start of each working day, although the albite standard and the VG568 rhyolite glass standard (Yellowstone National Park, Wyoming) were revisited regularly during analyses and before and after each sample to ensure there was no drift. Measurements on crystals were conducted with a focused ~1 μm beam with 20 nA current and 15 kV accelerating voltage. Analyses conducted on pseudotachylyte and interstitial glass in lithic clasts were conducted using a defocused 10 μm beam with 5 nA current and 15 kV accelerating voltage. Additionally, a defocused beam was also used to sample the bulk chemistry of areas of ultracataclasite. All tests with both focused and defocused beam had peak count times of 20 s and background (off peak) of 10 s.

In an attempt to obtain accurate and precise glass chemistries and minimise potential contamination from common restites (surviving crystals) in the pseudotachylyte glass, a 5 μm beam was also used for 6 analyses; they were found to return similar totals and chemistries to analyses done with the 10 μm beam.

In order to perform a rheological analysis of the frictional melt, the chemical composition obtained by EPMA was used as input in the GRD viscosity calculator (Giordano et al., 2008). ImageJ (Schneider et al., 2012) was employed to analyse phases in BSE images and estimate the crystal fraction as well as a maximum packing fraction, calculated following Mueller et al. (2010) and Klein et al. (2017). This data was input into the empirical relative viscosity calculator of Costa et al. (2009) to compute the rheology of the frictional melt suspensions.

4. Results

4.1. Field observations

During our field campaign, we surveyed the Arequipa volcanic landslide deposit and closely examined key structures. The deposit is characterised by a heavily eroded area of high topography extending 26 km west from Pichu Pichu in a broad, fan-like shape (Fig. 1). The upper surface of the deposit is draped by fall deposits of more recent volcanic activity in the area. Legros et al. (2000) originally estimated the volume of the deposit to be >10 km^3, however, with the deposit covering around 200 km^2 and thicknesses observed at >100 m even at distances >20 km

from the source, the volume could exceed even 20 km^3. Outcrops of the basal contact suggest a gentle 5° average slope of the original underlying topography. Current topography indicates that the central section of the deposit exceeds 300 m in thickness. An accurate estimation of the volume in this case is impossible due to the unknown basal topography, erosion of the deposit, poor mapping of the distal extent and a number of overlying fall deposits.

The deposit is cut by multiple rivers and their tributaries, including the Rio Socabaya in which localities 2 and 3 are found (Fig. 1). Locality 1 is situated in a different river-cutting near the Characato District. These incisions expose some of the internal flow structures developed during the debris avalanche. Here, we describe observations of key structures from three localities with extensive exposure. These include basal contacts, defining the paleotopography, as well as mid-body shear zones and clastic dykes.

4.1.1. Locality 1 – basal pseudotachylyte

Originally, the base of the debris avalanche deposit was observed in a river-cutting near Characato District to the SE of Arequipa (Legros et al., 2000), approximately 24 km from Pichu Pichu (Loc.1 see Fig. 1). Here,

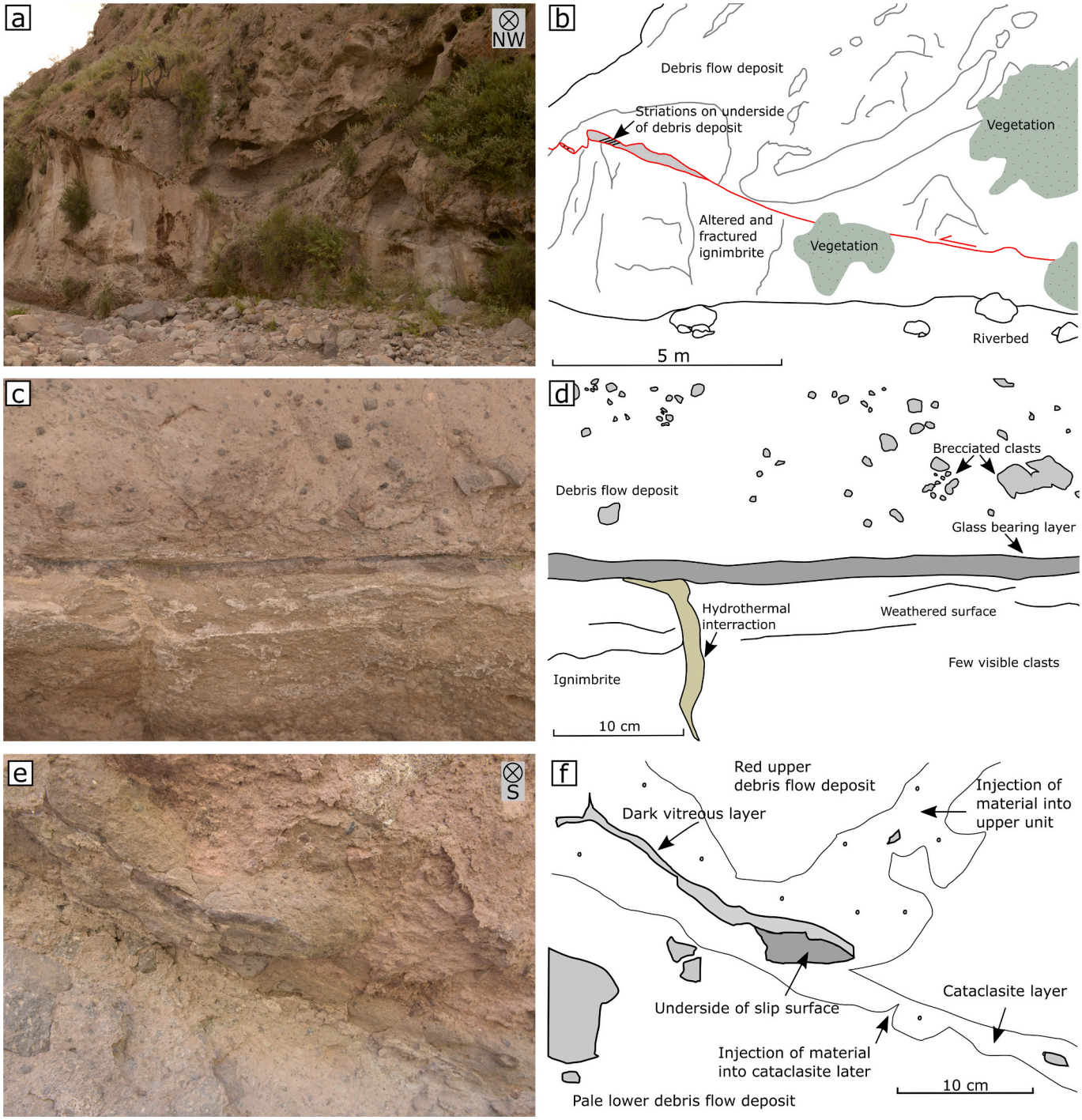

Fig. 2. Field photos and sketches of features at Locality 1. a-b) Basal contact of the debris flow with basal topology leading to extreme shear localisation. c-d) Close view of the basal surface with localised dark, vitreous, glass-bearing layer. e-f) Secondary shear zone 20 m above the outcrop in panels a–d showing juxtaposition of units separated by cataclasite plus a dark, vitreous seam.

the exposure presented by the river-cut is approximately 75 m long and 10 m high approximately parallel to the expected transport direction (Fig. 2a–b). Although the deposit extends further in all directions, vegetation covers most of the rocks on shallow topography. In this locality, the debris avalanche deposit is rather massive, made of a white-grey, granular medium consisting primarily of ash- and lapilli-size clasts of andesite lithics and individual crystals (Fig. 2a–b). The andesite blocks are porphyritic, containing 20% plagioclase (up to 2.2 mm), 15.3% amphibole phenocrysts (up to 2 mm), rarer pyroxene phenocrysts and a microlite-rich groundmass. The andesite blocks occasionally reach 30 cm in size within the deposit and often display jigsaw brecciation fracture patterns.

The underlying ignimbrite is exposed as a poorly consolidated and highly weathered rock of pale grey colour consisting of ash-sized grains without large lapilli. Crystals of both biotite and plagioclase are identifiable alongside dark lithic fragments but all are rarely larger than 1 mm in size. The rock is highly fractured and contains non-continuous veins of silicic hydrothermal material up to 1 cm thick (Fig. 2c–d).

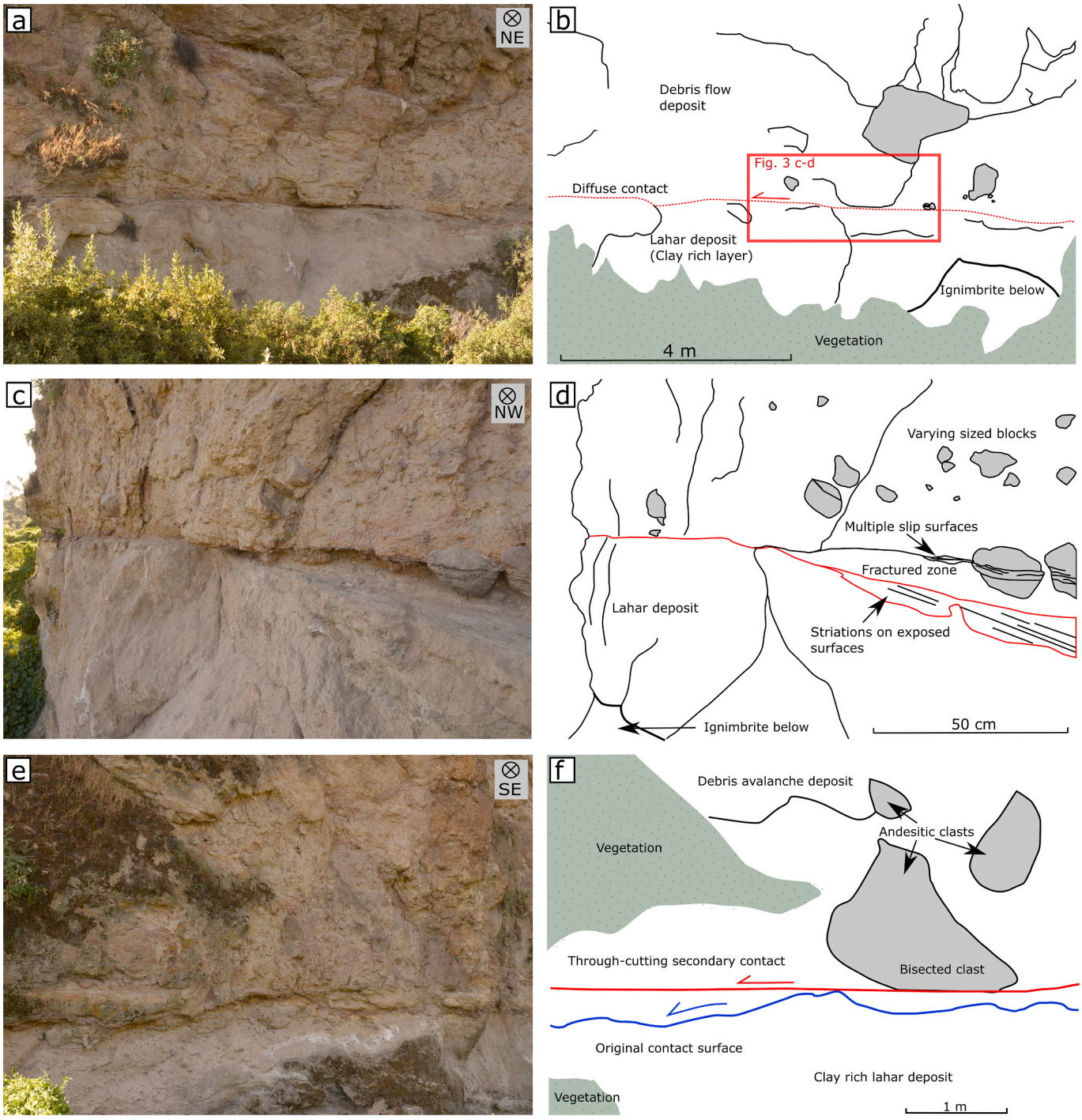

Fig. 3. Field photos and sketches from Locality 2. a-b) Debris avalanche deposit with large clasts and 40 cm thick diffuse basal contact. c-d) Closer view showing intense fracturing and cataclasis along the slip zone, multiple fractures cutting andesitic blocks in the fractured zone marked and striations on the lower slip surface. e-f) Basal contact 140 m west (downstream) showing how rough topology of the original contact (blue) is superseded by a secondary through-cutting contact (red) that also bisects a clast. (For interpretation of the references to colour in this figure legend, the reader is referred to the Web version of this article.)

These veins all follow a similar orientation, striking in a 014–020 direction with high dip angles of 80-90° to the east, following the orientation of regional tectonic features (Lebti et al., 2006).

The contact between the debris deposit and the underlying basal ignimbrite is sharp, consisting of a thin, dark grey, vitreous layer approximately 1–1.5 cm thick (Fig. 2c–d). The contact is observed at an elevation of 2610–2620 m in the northern face of the river-cutting and is dipping away from the outcrop face towards the north (strike 090 and 091) at variable angles, but generally around 35°(Fig. 2a–b). The contact visibly extends over a length of ca. 60 m and is curvilinear, increasing in elevation by approximately 4–5 m over a distance of approximately 10 m away from Pichu Pichu at this locality. Overhanging areas of the upper slip surface at the base of the deposit exhibit striations trending 286° which deviates approximately 25° north from the expected flow direction. The material either side of the contact is highly brecciated, containing no fragments larger than 4 cm within 50 cm of the contact.

4.1.2. Locality 1 – intra-body shear zone

Strain localisation was not restricted to the basal contact at Loc. 1. An additional shear zone was identified within the deposit, some 20 m above the basal contact at 2636 m elevation and 30 m due NE from the basal contact previously described. Here, a change in colour is noted above and below the shear zone. The lower unit is a pale grey colour, fine-grained breccia, similar to that described directly above the basal contact but with rare larger (>20 cm) andesitic blocks. Above is a breccia with red-coloured matrix, rich in andesitic blocks (Fig. 2e–f). The clasts in this upper lithology are larger, up to 50 cm, with less jigsaw brecciation and more angular shapes. These two units are separated by a layer of light brown material with no large clasts that varies from 2 to 10 cm thick and which is seen to inject into the lithology above. Within this, there is a thin layer of dark, microcrystalline material, approximately 3–4 mm thick (Fig. 2e–f). The shear zone is observed to extend laterally for approximately 45 m and runs sub-parallel to the basal contact below at a strike of 108° dipping to the north by ~20°.

4.1.3. Locality 2 – cataclastic basal contact

A new exposure of the deposit base was found to the northeast of the original locality in a different river valley, approximately 17.5 km from Pichu Pichu (Loc. 2 see Fig. 1). Here, the materials forming the debris avalanche deposit and the underlying ignimbrite remain the same as in Loc. 1, yet the upper surface of the ignimbrite is, in some laterally discontinuous sections, draped by a 1–2 m thick layer of more clay rich, lahar deposit material with some imbrication of small clasts. The nature of the contact is however different and varies laterally within the outcrop, which totals approximately 300 m along a river-cutting (Fig. 3). The contact, observed at an elevation of 2854–2858 m, is seen in the north face of the river-cutting, near-parallel to the flow direction and is generally linear and almost horizontal (Fig. 3a–b). It is largely visible as a sharp boundary between the two units (with either the thin lahar layer or ignimbrite as the lower unit). A large clast is preserved near the base of the debris avalanche, cut by multiple well-defined fractures parallel to the primary contact (Fig. 3c–d). In this locality, no vitreous layer is present, but the shear zone contains extremely fragmented, fine, angular material and displays red iron oxide stains and 303° trending striations on the lower contact surface with the lahar (Fig. 3c–d). This is a more northerly direction of flow, due to the fanning of the deposit across the land surface.

140 m to the west, separated from the previously described outcrop by an area of vegetation, an undulating contact is visible between the debris flow and the ignimbrite material where troughs were present in the paleotopography (i.e., the upper surface of the ignimbrite; Fig. 3e–f). The deposit filled the depression and exhibits diffusely distributed alignment of material (akin to inclined sub-parallel laminations) up to a sharp slip surface that crosscuts the debris avalanche deposit (Fig. 3e–f). Here, the base of a >2 m large andesitic clast is flat and parallel to the primary slip surface, showing signs of a throughgoing, bisecting rupture. No vitreous layer is present in the shear zone at this locality.

4.1.4. Locality 3 – intra-body shear zone and clastic dykes

In the Rio Socabaya gorge (Loc. 3 see Fig. 1), river incision exposes a >800 m long, up to 100 m high section of the debris avalanche deposit on both sides of the river valley. Here, the deposit is made of a massive, white-grey, granular medium consisting primarily of ash- and lapilli-size clasts of andesite lithics and crystals. However, in this locality, rare larger blocks of andesite were observed in the deposit up to 3–4 m in size. There is no visible basal contact between the facies identified, though the ignimbrite is exposed approximately 200 m to the west. Instead, the main rock mass exhibits multiple clastic dykes as well as intra-body shear zones some 5–10 m above the river bottom. The structurally-lowest shear zone, identified at the western end of the southern bank, developed within the main body of rock and does not separate disparate units within the debris avalanche deposit (Fig. 4). The shear zone appears as a linear feature marked by a thin, microcrystalline layer some 0.5 cm thick and extending over a length of approximately 5 m. The layer is not straight, but rather undulose. There is no discernible variation in clast shape or size in relation to the shear zone, though it is often obscured by vegetation. A few metres to the west of the end of the visible shear zone there is a clastic dyke, 2 m thick and >10 m high intruding sub-vertically into the deposit.

Multiple clastic dykes have been injected into the debris deposit from below, though the source of the material is not observed in the field. These structures range in size from 10 cm to 2–3 m in thickness and reach up to several tens of metres in length (Fig. 5a–b). The thickness of the larger clastic dykes changes along their length, generally tapering towards their tips. Most of the dykes are sub-vertical, but there are several occurrences of sections of dykes, locally projecting horizontally around large, metre-scale clasts. The edges are sharp with the deposit, and material entrained in the clastic dykes varies in size and prevalence. The majority of the dykes contain predominantly fine-grained clastic material with small lithic clasts (mostly andesitic) and crystal fragments. In one case, a dyke contained over 50% mass of clasts (in a fine-grained groundmass), varying in composition and 1–30 cm in size. The margins of this dyke are devoid of large clasts, are fine-grained and show evidence of laminar shear banding (Fig. 5c–d). In other cases, the dykes do not show evidence of internal strain localisation or gradational deposition. The dykes are intact and do not exhibit any offset, anticipated from post-emplacement shear within the bulk of the avalanche, indicative of their late stage occurrence.

A second site observed in the same river valley is a shear zone consisting of a near-planar feature through the deposit exposed on the inside bend of the southern bank. This shear zone is approximately 25 m in length, with no discernible variation in lithology on either side. There is an observed reduction of the number of clasts above 3 cm in a layer 20 cm in thickness above the planar feature (Fig. 6), though intermittent large clasts up to 50 cm in size are present. At this shear zone the planar feature is additionally highlighted by its interaction with the clastic dykes. A dyke propagating from below terminates at the shear zone, increasing in width from 1 m to 3 m at the intersection, visible in the outcrop and extending several metres along the shear plane, gradually pinching out. 3 m to the west of the large clastic dyke, another dyke, 30 cm in width cuts across the planar shear zone into the unit above (Fig. 6).

4.2. Microstructural analysis

Thin sections of sheared samples were made perpendicular to shear and parallel to the slip vector. Micro-textural analysis was performed using optical microscopy and BSE imagery.

4.2.1. Locality 1 – pseudotachylyte basal contact

Microtextural analysis of the basal contact at Loc. 1 reveals that the dark layer observed at outcrop scale comprises a 12 mm thick vitreous

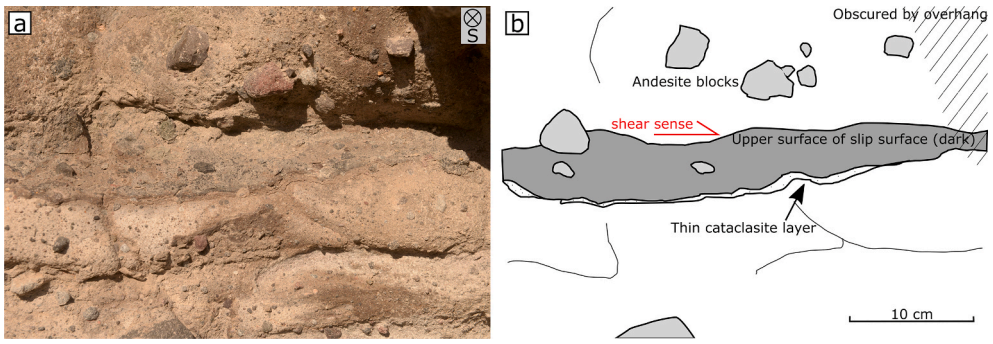

Fig. 4. Field photo and sketch of a secondary shear surface within the debris avalanche at Locality 3 bounded by a thin layer of very fine cataclasite. The outcrop is oblique to vertical, revealing the top surface of the cataclastic vein. Moderately large clasts and blocks are present either side of the boundary, with shear indicators largely absent.

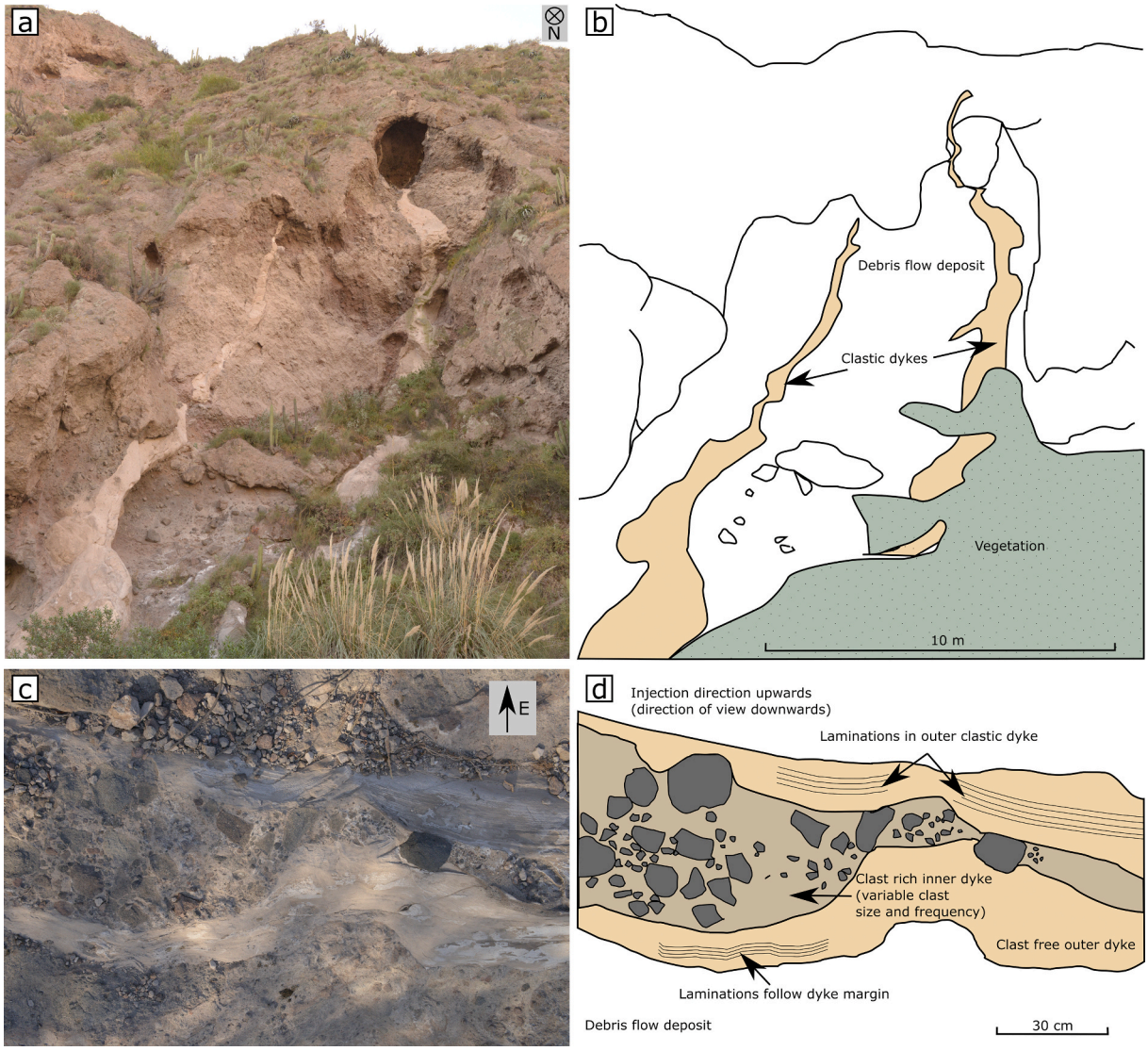

Fig. 5. Field photos and sketches of Locality 3. a-b) Clastic dykes with variable thickness (0.05–1.5 m) injected up to 20 m sub-vertically into the debris avalanche deposit with sharp, undulating boundaries. c-d) Clast rich (primarily andesitic) clastic dyke located 80 m east of that shown in a-b, with larger clasts in the centre and a fine grained boundary. The direction of injection is upwards.

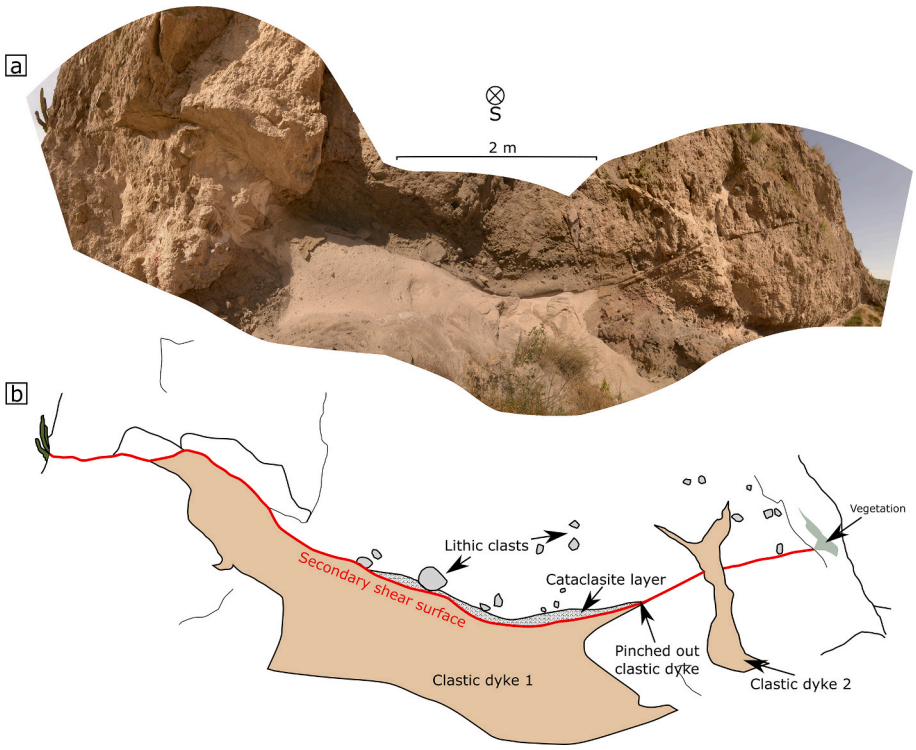

Fig. 6. Stitched panoramic field photo and sketch of secondary shear surface interaction with clastic dyking at Locality 3. A large clastic dyke initiated from the primary basal slip surface below (not shown) terminating at the linear secondary shear surface feature in the outcrop. A second clastic dyke to the right of the image cross-cuts this linear feature with no displacement.

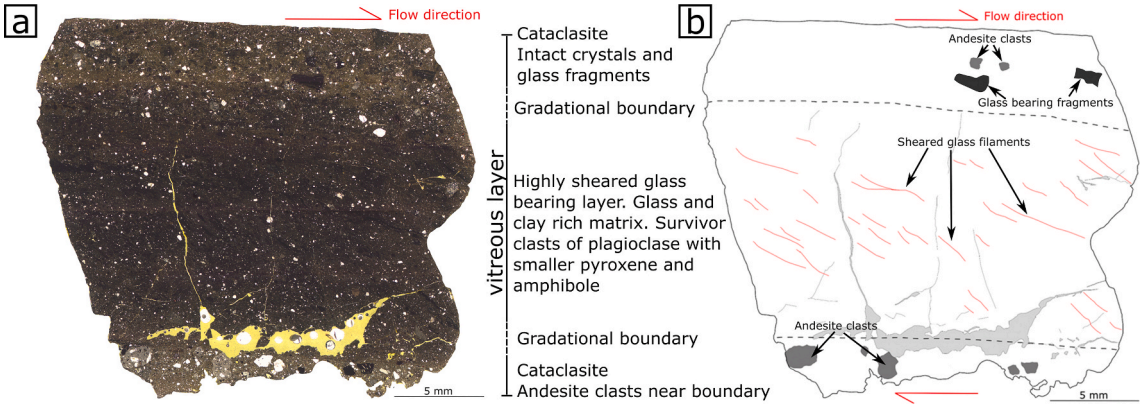

Fig. 7. Thin section photomicrograph (in plane polarised light) showing the full thickness of the glass-bearing basal layer from Loc. 1. The layer is bounded by cataclasite and separates andesitic debris avalanche deposit above and the ignimbrite below (not shown here). A dark, glass bearing central layer contains sheared glass filaments (black areas, annotated with red lines in sketch), ultracataclasite (brown areas) and survivor clasts. The bounding cataclasite contains coarser crystal, lithic and relict melt fragments (thin section PPA1_1.1). (For interpretation of the references to colour in this figure legend, the reader is referred to the Web version of this article.)

layer with ~3 mm thick undulose, and diffuse boundaries at the top and bottom to cataclasites, which contain lithic clasts of bounding lithologies up to 2 mm in size (Fig. 7).

Visual observation of the central dark vitreous layer shows that it is made of a mix of tortuous (fluidal) black isotropic filaments (in plane-polarised light), up to 0.7 mm thick and 5 mm long, and a large fraction (around 40%) of a dark brown material consisting of identifiable small rock fragments and crystals (Fig. 7). SEM image analysis reveals the black isotropic filaments to be bubble-bearing material with no identifiable crystal structure (Fig. 8). Later EPMA analysis produced consistent chemistry, ruling out the presence of small crystals. Therefore, as identified in Legros et al. (2000), the isotropic black material is interpreted to be glass, with interspersed ultracataclastic, crystal-rich dark brown material. The glass filaments contain varying fractions of vesicles (Fig. 8a–b) which are up to 8 μm in size and occasionally elongated in the direction of en-echelon alignment of the melt filaments. Where preserved around large clasts, elongate vesicles form trails following the direction of shearing. Within the filaments, small, rounded patches of silica (5 μm) are observed.

In the brown material the crystals are predominantly plagioclase feldspar up to 0.6 mm in size with a modal size <0.4 mm. They show as equant fragments with multiple fractures. Additionally, smaller pyroxene crystals and occasional hornblende (<0.1 mm) are observed but are concentrated on the outer edges of the dark, vitreous layer. SEM image

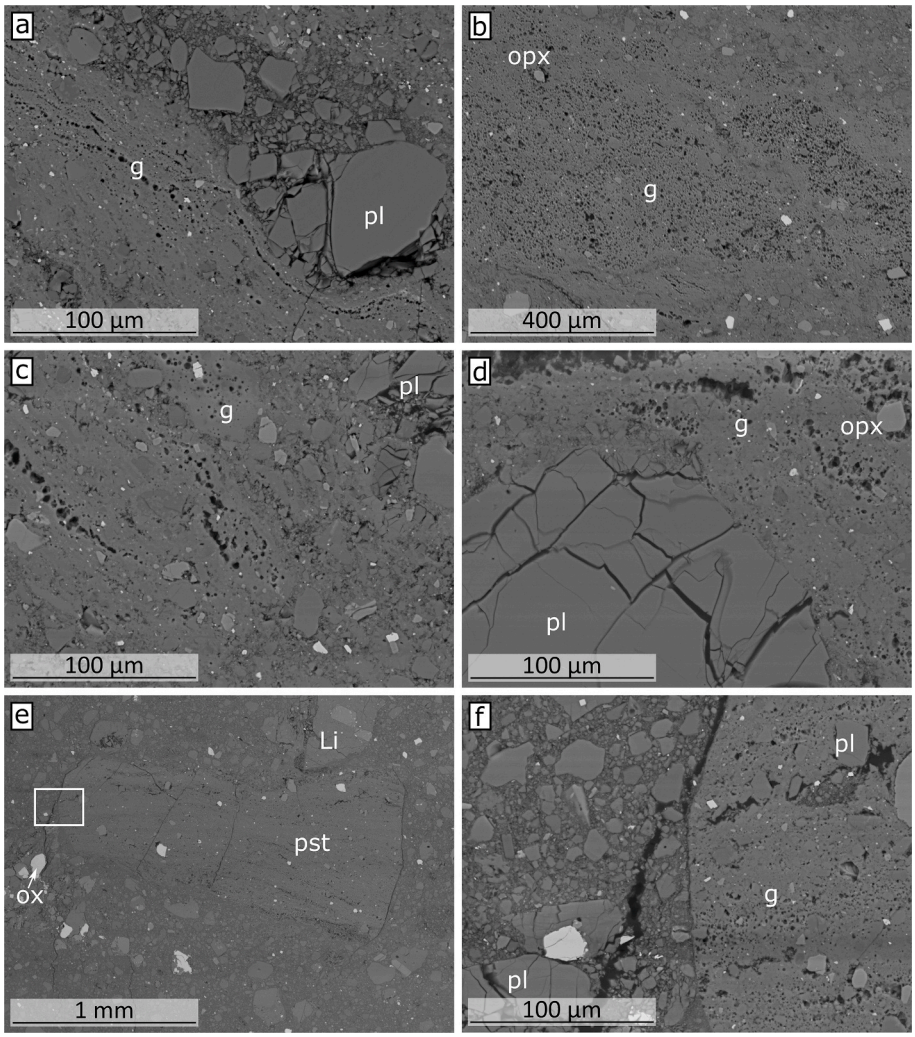

Fig. 8. BSE images of the vitreous basal layer from Loc. 1 (also shown in Fig. 7). a) A sheared and fractured plagioclase clast within the glass-bearing layer. b) Vesicular glass in the primary slip surface with stretched bubbles along the lower boundary indicating shear. c) Sheared and vesicular glass and ultracataclasite, following Riedel shear directions. d) Fractured plagioclase survivor clast within the preserved glass bearing layer. e) Glass-bearing pseudotachylyte fragment within the cataclasite (box shows position of f). f) The rounded margin of the pseudotachylyte fragment with intermixed layers of ultracataclasite and glass, within the granular cataclasite. pl = plagioclase, g = glass, ox = oxides, opx = orthopyroxene, Li = lithic clast, pst = pseudotachylyte clast (thin section PPA1_1.1).

analysis reveals that the larger clasts have extensive cracking (Fig. 8d) but remain together forming a brecciated texture. The fractured and sheared plagioclase crystals (Fig. 8a and c) form elongate layers of plagioclase-dominated fragments.

The layering between pseudotachylyte glass and ultracataclasite follows Riedel shear bands concordant with the shear in the flow direction (Fig. 7). The darker, glass-rich filaments are more predominant in the centre of the layer and are absent from the bounding cataclasite. In these marginal cataclastic zones (separating glass layer from the andesite above and ignimbrite below), we observed large clasts consisting of fragments of mixed vesicular pseudotachylyte-ultracataclasite banded materials (pst in Fig. 8e–f), similar in texture to the intact vitreous layer. The fragments are further fractured (showing trivial offset) and the margins are sub-angular.

4.2.2. Locality 1 – intra-body shear surface

The intra-body shear plane approximately 20 m above the basal contact at Loc. 1 is dominated by the presence of clasts and microcrystalline material. The visibly pale layer in the outcrop is a poorly sorted clast rich cataclasite, the dark vitreous layer is denser ultracataclasite welded with small amounts of amorphous material between grain contacts (Fig. 9a). The largest clasts observed here are andesitic, 5–6 mm in size and semi-rounded, which are larger than the clasts near to the basal contact hosting frictional melt (section 4.2.1). Smaller crystal fragments, primarily of plagioclase are also present (Fig. 9b). In addition, the contact between the cataclasite and the thin, denser ultracataclasite layer is sharp (Fig. 9b–c).

4.2.3. Locality 1 – basal ignimbrite

Analysis of the ignimbrite below the contact at Loc. 1 found that the formation is rich in similar sized anhedral plagioclase and sanidine crystals, commonly 1–2 mm in size and up to 3 mm with occasional smaller quartz and biotite crystals up to a maximum of 1 mm in size (Fig. 10a). The plagioclase and sanidine crystals occasionally form glomerocrysts containing a combination of the two most abundant phenocryst types. These crystals are hosted in a matrix of small needle-shaped glass shards, (<0.5 mm). In the sample collected there is no evident welding of the material, which has high porosity. The crystal assemblage matches that described for the La Joya Ignimbrite formation mapped within the Arequipa basin infill, which is thought to extend across the whole area below the debris avalanche deposit (Lebti et al., 2006).

4.2.4. Locality 2 – cataclastic basal contact

From the basal contact at Locality 2, there is no evidence of the localisation of shear onto a single zone. Instead, the material across a band of approximately 40 cm thickness is formed of highly fractured lithic and crystalline fragments and clasts hosted in a matrix of clay (Fig. 10c) with no evidence of glass. Larger lithic fragments, ranging in size from <1 mm up to 7–10 mm in size, are identifiable as andesitic in composition with similar crystal content as clasts from Loc. 1, with abundant sub-euhedral plagioclase (<1 mm) and subhedral amphibole

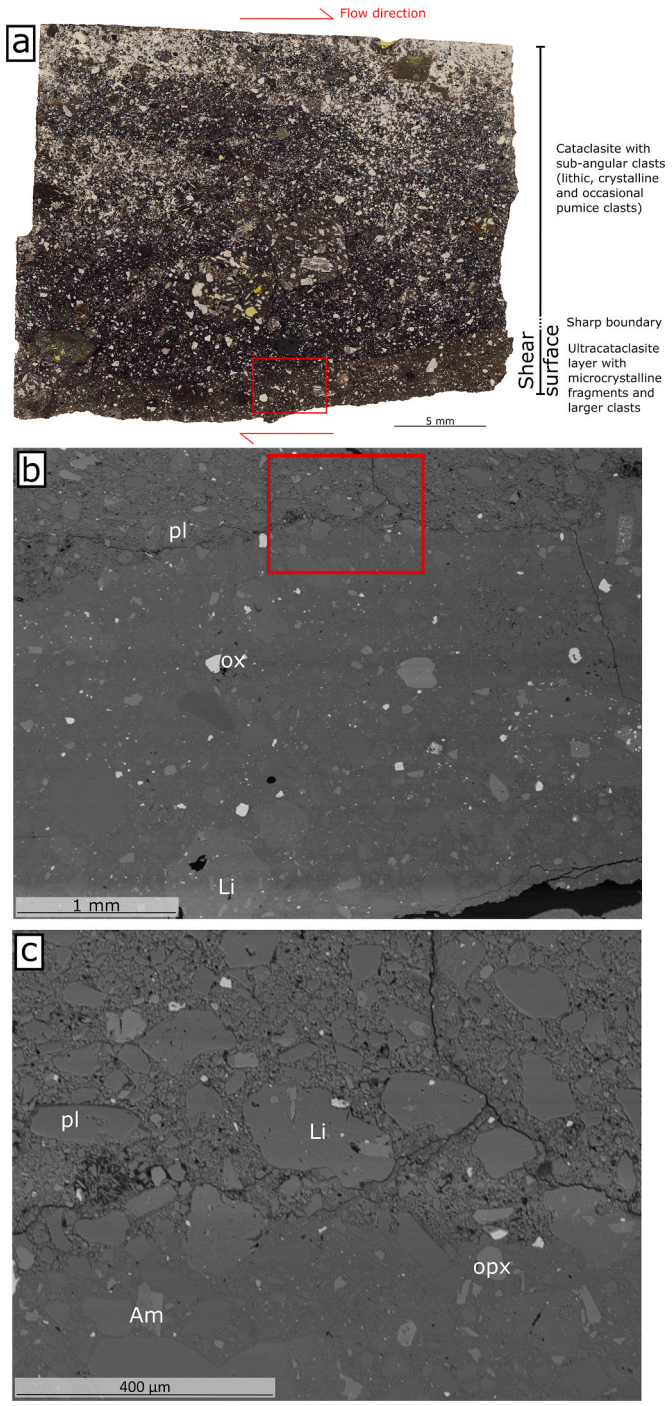

Fig. 9. Thin section from secondary slip surface at Loc. 1. a) A PPL photomicrograph showing cataclastic textures (clasts >0.5 mm) with darker brown ultracataclasite making up the primary shear layer at the base (red box shows area in b). b) BSE image of the granular cataclasite above the denser ultracataclasite (red box shows area in c). c) The cataclasite and ultracataclasite show similar components (crystal and lithic clasts) but are distinguished by an abrupt porosity contrast (thin section PPA1_5.3). (For interpretation of the references to colour in this figure legend, the reader is referred to the Web version of this article.)

phenocrysts (<0.8 mm). Plagioclase forms the largest of the crystalline fragments in the shear zone, though small, subangular, amphibole and biotite crystals around 1 mm in size are also observed in the cataclasite. Several large pumiceous clasts up to ~4 cm in size are also preserved within the shear zone with only minor fracturing. These pumiceous clasts contain plagioclase, sanidine and biotite. Small fragments are often monocrystalline, commonly plagioclase up to 2 mm in size. The orientation of these fragments shows no evidence of Riedel shearing and there are no pervasive shear fabrics observed within the cataclasite.

4.2.5. *Locality 3 - clastic dyke*

A sample of a large clastic dyke in the northern face exposure at Loc. 3 is observed to contain considerable fractured glassy pumice fragments, andesite clasts (up to 7 mm in thin section though field observations indicate larger clasts are present), individual crystals of plagioclase and a high clay content (Fig. 10b). Additionally, some biotite (tabular, up to 1 mm) is present, which is not observed in the lithologies of the debris avalanche but is observed in the ignimbrite and cataclastic basal shear zone.

4.3. *Geochemical analysis*

Geochemical analysis was performed to reconcile physico-chemical processes associated with the evolution of shear and frictional melting. XRF analysis was used to constrain the chemical composition of the host rocks, confirming the andesitic nature of the avalanche deposit and the rhyolitic chemistry of the ignimbrite (Fig. 11, see supplementary data).

EPMA was conducted on several mineral phases from host rocks and crystal fragments and amorphous areas from the basal layer at Loc. 1 to constrain the development of frictional melting (with respect to the host lithologies). The plagioclase crystals in the vitreous layer as well as in andesite lithics within the ultracataclasite and ignimbrite host wall rock are compositionally grouped (Fig. 11), with CaO ranging from 6 to 9 wt % and NaO from 6 to 8 wt% (see supplementary data). Amphibole crystals in lithic fragments as well as rare individual crystals in the ultracataclasite at Loc. 1 were found to be compositionally similar and were absent in the vitreous layer (Fig. 11, see supplementary data). The two types of pyroxene present in the andesite, cataclasite and vitreous layer, were identified as augite (clinopyroxene; Ca-rich) and enstatite (orthopyroxene; Mg-Fe rich).

Glasses in both the preserved vitreous layer and in a fragment of glass-bearing material found in the cataclasite were analysed (Fig. 8). The EPMA chemical composition of glass from the basal pseudotachylyte plots between the XRF bulk chemistry of the underlying ignimbrite and the andesitic blocks from the debris avalanche deposit (Fig. 11). The glass however tends to be enriched in SiO_2, plotting closer to the composition of the ignimbrite than that of the andesite. In contrast, the glass fragments preserved in the marginal cataclasite of the basal shear zone spans a wider range in chemistry that is notably more mafic in composition. The glass in these pseudotachylyte fragments has less CaO wt% and SiO_2 wt% than either the andesite or the ignimbrite (Fig. 11b). Analyses on the ultracataclasite within the layer returned poor totals with highly varying chemistries, suggesting sampling of mixed lithology fragments.

5. Interpretation

The field, microstructural and geochemical data can be used to make several interpretations about the mechanics of shearing within the debris avalanche.

5.1. *Intergranular forces and fragmentation*

The contrasting nature of the different basal shear zone exposures provide clues as to the emplacement mechanisms. At the basal contact at Loc. 1, we do not observe large andesitic clasts within 5 m of the contact and there is evidence of intense brecciation (Fig. 2). In comparison, at Loc. 2 we observe a number of large andesitic clasts, up to metre scale in close proximity to the basal shear localisation zone (Fig. 3). This

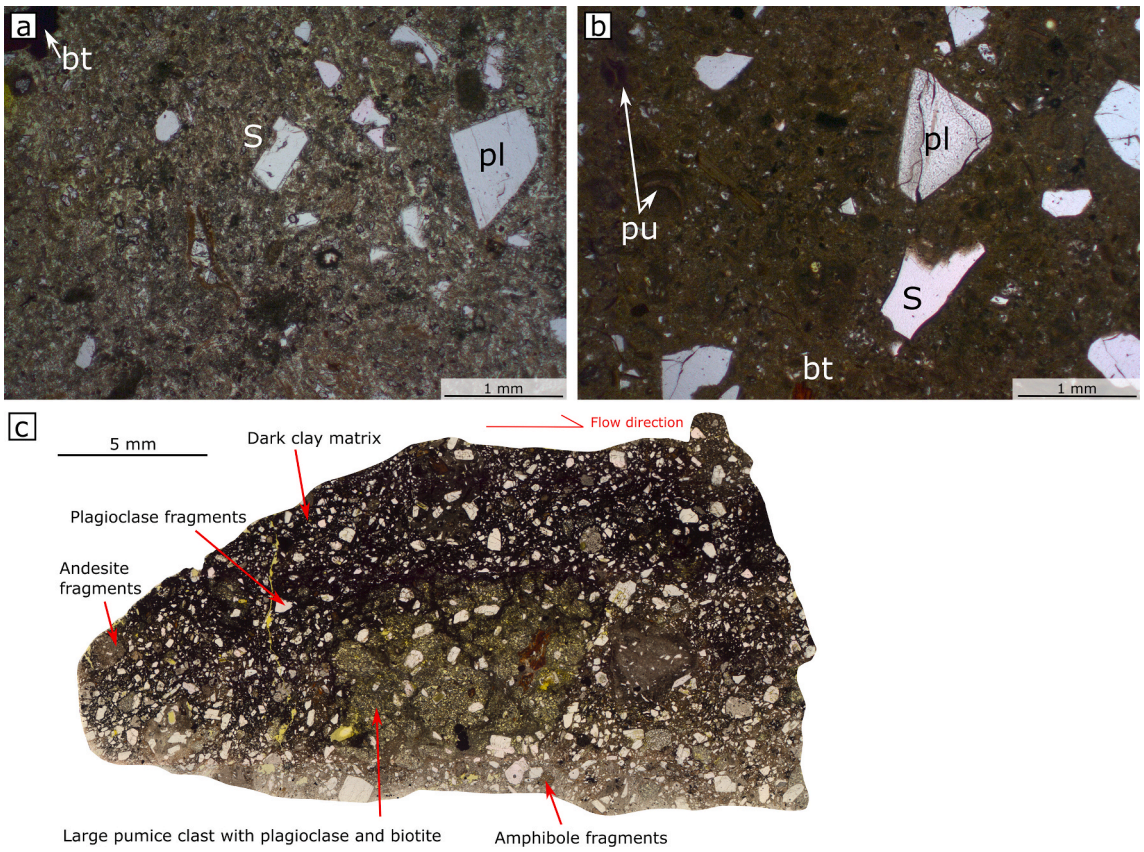

Fig. 10. PPL photomicrographs illustrating mineralogy of a) Porous ignimbrite from Loc. 1 with sanidine (S), plagioclase (pl) and biotite (bt) crystals in a glass shard matrix (thin section PPA1_1.1). b) Clastic dyke from Loc. 3 with sanidine, plagioclase, biotite and pumice (pu) shards with high clay content in the matrix (thin section PPA2_2.1). c) The cataclastic basal shear zone at Loc. 2 hosts a range of clasts of different size and composition (thin section PPA3_2.1).

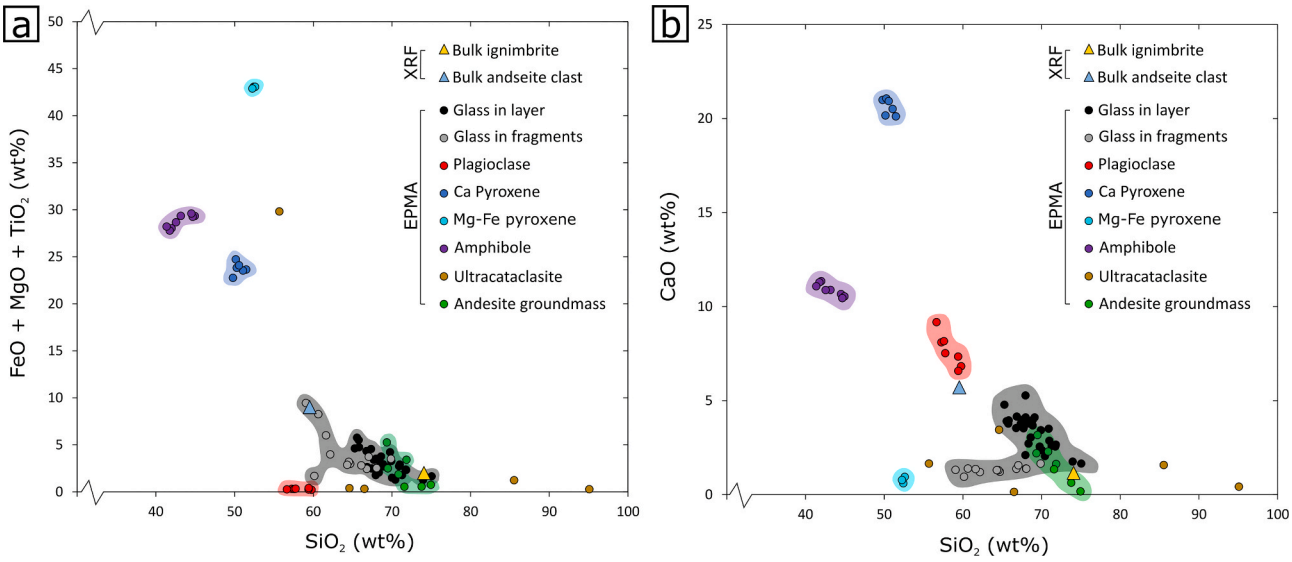

Fig. 11. Chemical analyses by XRF (triangles) of an andesite clast from the debris avalanche and ignimbrite from Loc. 1, and chemical analyses by EPMA of the glass within the pseudotachylyte layer from Loc. 1, as well as plagioclase, amphibole, pyroxene and the groundmass from 3 andesite clasts and plagioclase and biotite from the ignimbrite, plotted as: a) Mafic (FeO + MgO + TiO_2) wt% against silicon dioxide (SiO_2) wt% showing relation of frictional melt (glass) to bulk chemistry and individual minerals; and b) Calcium oxide (CaO) wt% against SiO_2 wt%, with low CaO wt% suggesting involvement of andesitic enstatite (Mg-Fe pyroxene) in generation of the fragmented glass. (For interpretation of the references to colour in this figure legend, the reader is referred to the Web version of this article.)

suggests greater intergranular forces may have occurred near the base of the flow at Loc. 1 compared to Loc. 2 that exceed the elastic limit of the clasts (Davies and McSaveney, 2009), resulting in intense fracturing and reduction in clast and particle sizes (Arabnia and Sklar, 2016). This qualitative observation can also be made at a smaller scale within the shear localisation zone itself, where centimetre-scale clasts at Loc. 2 have survived (in comparison to the smaller fragments in the glass-bearing layer at Loc. 1). Some of these fragments are pumiceous (Fig. 10c) material that, due to their highly vesicular nature, would be mechanically weaker than other crystalline and lithic fragments. Their survival means that there was less cataclastic damage associated with this shear zone. The inferred greater intergranular forces at Loc. 1 also enhances the ability for frictional heating (Carslaw and Jaeger, 1959) that can lead to melting. In support of this, biotite and amphibole fragments present in the cataclasite (Figs. 9 & 10c) are absent in the vitreous pseudotachylyte (Figs. 7 and 8), suggestive of selective melting of the mineral assemblage due to the lower fracture toughness and melting temperature of these phases (Spray, 2010).

5.2. Transient nature of slip zones and slip zone morphology

Despite the deposit only preserving the cumulative history and final state of the debris avalanche, there is evidence to suggest the temporal evolution of the basal shear zones during the flow of the debris avalanche. At Loc. 1, the presence of glassy fragments in the cataclasite bounding the glass-bearing pseudotachylyte layer (Figs. 7 & 8e-f) suggests that there were at least two melting events. The "glass in layer" and "glass in fragments" have different textures and chemistry (Figs. 8 and 11) so either formed from different mixtures of material in the basal shear zone or under different temperatures, timescales and slip conditions. The original layer became fractured and subsequently a new layer comprising ultracataclasite and pseudotachylyte was formed. This process may have occurred multiple times throughout deposition. The development of a secondary slip layer at this locality was likely a late stage development, potentially induced by the slowing of the lower portion of the flow by loss of momentum and interaction with topography.

Similarly, at Loc. 2, the initially rough topography of the basal contact is cut through by a secondary linear contact (Fig. 3e–f) suggesting gradational shifts in slip rate or overburden to localise slip to different surfaces at different times. Additionally, multiple fractures splay from these surfaces and cross-cut within the shear zone (Fig. 3c–d) suggesting distinct ruptures.

Within the body of the avalanche deposit at Loc. 3, clastic dykes interact with a linear localised shear plane (Fig. 6). The dyke is wider and contains evidence of shear at the contact with the shear plane, indicating it may have terminated at the shear zone during active slip on that contact. In contrast a second clastic dyke at this locality injects through the preserved linear shear plane and is not subjected to any displacement along the shear plane. Therefore, this dyke must have occurred after shearing on this secondary shear plane ceased. This interaction of dykes and shear surfaces is additional evidence supporting the transient nature of active shear surfaces both at the base and within the flow.

5.3. Melt chemistry and source rocks

The chemical analyses for the frictional melt glass at Loc. 1 plot between the two bulk rock chemistries of the lower ignimbrite and andesitic upper plate material (Fig. 11). This suggests that a combination of both materials, initially incorporated and sheared in the basal zone, melted to form the glass preserved in the intact basal shear zone.

The more mafic composition of the analysed frictional melt glass fragments within the cataclasite (Fig. 11a), interpreted as remnants of a previous melt-producing shear zone, is likely due to early melting of amphibole and biotite (present in the host rocks and cataclasites). This is also supported by the highly vesicular nature of these fragments, as melting of hydrous phases releases water (e.g. Magloughlin, 2011). Primitive or partial frictional melts are frequently more mafic than more mature melts (Wallace et al., 2019 and references therein) and leave suspended survivor clasts of minerals with higher fracture toughness and/or melting temperature (Spray, 2010). Further melting of the more resistant minerals brings the melt chemistry back towards the bulk chemistry, as seen here with the chemistry of the intact basal pseudotachylyte composition which plots between the andesite and ignimbrite.

5.4. Frictional melt rheology evolution

Understanding the development and impact of frictional melting on the debris avalanche requires consideration of its rheology. Here the observations that slip caused frictional melting as well as fragmentation of frictional melt are used to constrain conditions in the debris avalanche during runout. We used the geochemical compositions of the glass (from the preserved layer and the fragment of glass-bearing earlier melt identified within the bounding cataclasite, both from the basal contact at Loc. 1) as input parameters in the GRD viscosity calculator of Giordano et al. (2008) to constrain the temperature (T in Kelvin) dependence of the viscosity (η in Pa s) of the early frictional melt present in fragments (η_e) and late frictional melt forming the main basal pseudotachylyte (η_l):

$$log\eta_e = A + \frac{B}{T(K) - C} \quad (1)$$

Table 1 provides the values of A, B and C (where B and C are adjustable parameters controlled by composition and A is a constant independent of composition related to the viscosity at infinite temperature, see Giordano et al. (2008)) to model both melts (Fig. 12a). The chemical compositions vary significantly locally due to the presence of small unhomogenised melt filaments (schlieren), which would have contrasting rheologies. However, the chemical compositions input do not include the water concentrations which would have likely been transiently present in the frictional melts owing to the presence of amphibole in the host rock (e.g. Wallace et al., 2019). Here, we assume the melt phase contained a nominal 0.1 wt% water concentration in this low-pressure environment.

The frictional melts described here contain variable fractions of suspended crystals and bubbles, known to impact the rheology and contribute to a non-Newtonian behaviour (Caricchi et al., 2007; Lavallée et al., 2007; Truby et al., 2015; Coats et al., 2018). Here we consider the influence of crystals (i.e., fraction, shape and maximum packing) using the two-phase rheology calculator from Costa et al. (2009). We first constrained the solid fraction present in the pseudotachylyte (i.e., surviving crystals and lithics) via SEM image analysis using the ImageJ online toolbox (Schneider et al., 2012). We estimated the solid fraction in the early pseudotachylyte at 0.25 and late pseudotachylyte at 0.43 and the aspect ratio of the particles as 1.761 in the early and 1.684 in the late pseudotachylyte. Then, following guidelines from Mueller et al. (2010), we used the aspect ratio of the solid fraction to define a critical maximum packing of a monodisperse distribution ($\phi_{m,m}$) for both suspensions at 0.57. However, due to the polydispersivity (δ) of the solid fraction, the true maximum packing is higher. We used the method of Phan et al. (1998) to define the polydispersivity where $\delta = \frac{r_{sd}}{r}$ where r_{sd} is the standard deviation of the fragment radii (3.00 and 2.71 for the fragment and layer respectively) and r is the mean of the fragment radii (3.66 and 3.67 for the fragment and layer respectively). This is based on measurements from 205 particles from the glass bearing fragment and 417 particles in the preserved layer over an analysis area of 200 and 100 μm^2 respectively (see supplementary data). Subsequently, the polydispersivity in the fragment (δ_e) and later preserved layer (δ_l) pseudotachylytes were input into the fitting equation from Klein et al. (2017) substituting the monodisperse maximum packing of spheres ($\phi_{m,0}$) for our previously defined monodisperse packing of the solid fraction's

Table 1
Values for variables A, B and C used to determine melt viscosity with Eqs. (1) and (2). Min and max represent compositional ranges from low to high (respectively) SiO_2 concentration of the glass-bearing layer and fragment. The values of A, B and C are used to constrain the viscosity of each frictional melt (η) and apparent viscosity of each suspension (at a strain rate of 10^3 s^{-1}) at a nominal temperature of 1250 °C.

Sample	A		B		C		$log\eta$ at 1250 °C		$log\eta_{app}$	
	Min	Max	Min	Max	Min	Max	Min	Max	Min	Max
Layer	−4.55	−4.55	9126.4	11264.3	406.7	304.8	3.62	4.69	4.34	5.42
Fragment	−4.55	−4.55	8681.8	10666.0	421.2	332.4	3.33	4.41	3.67	4.75

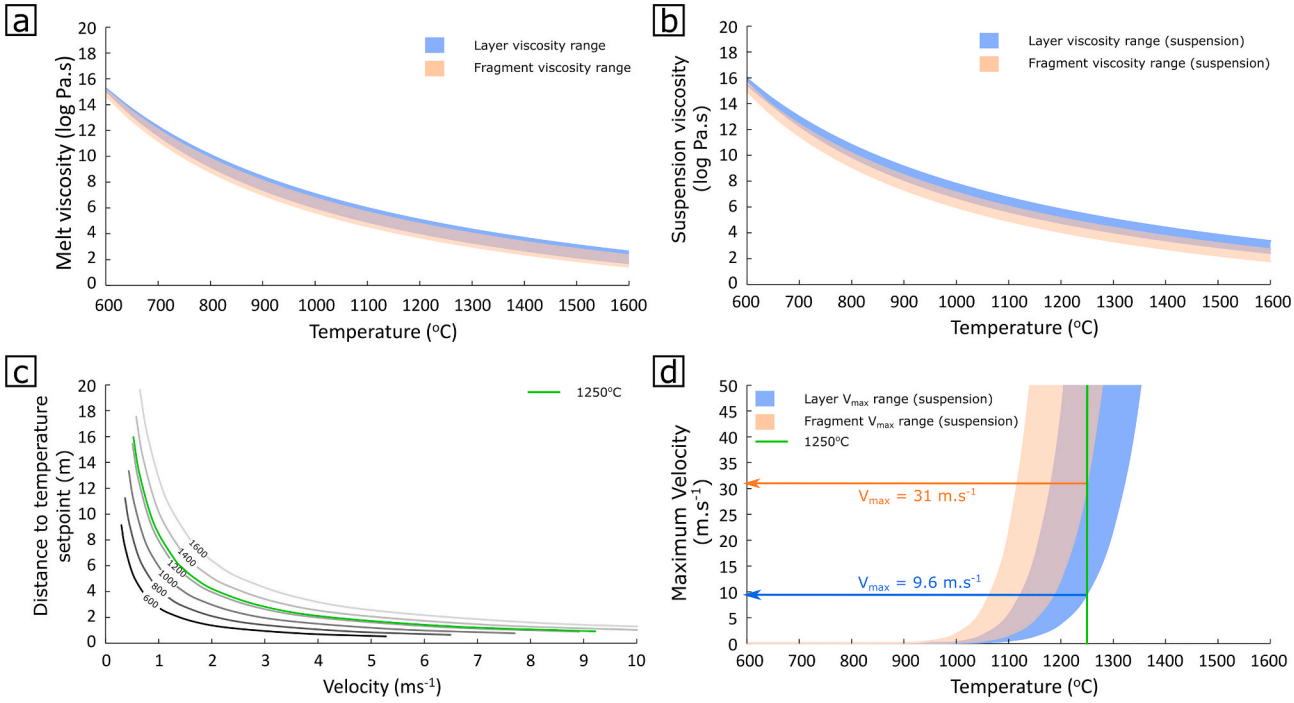

Fig. 12. Modelling the generation and rheology of the frictional melts. a) Temperature-viscosity relationships of the glass in the preserved layer (blue) and fragment (orange), using Eqs. (1)–(2). b) Temperature-viscosity relationships of the preserved layer and fragment considering the suspended solid fraction and bubbles, using Eq. (9). c) Slip distance required to produce heating of a given magnitude (contours) for different slip velocities, using Eq. (3), showing the estimated maximum temperature, 1250 °C (green). d) Maximum possible velocity experienced by the modelled suspensions avoiding brittle failure. Presence of fragments suggests velocity exceeded 31 ms^{-1} at 1250 °C and melting persisted to form the preserved layer. (For interpretation of the references to colour in this figure legend, the reader is referred to the Web version of this article.)

aspect ratio ($\phi_{m,m} = 0.57$). This defines the true maximum packing of the solid fraction of the early fragment ($\phi_{m,e}$) and late preserved layer ($\phi_{m,l}$) such that:

$$\phi_{m,e} = (1 - \phi_{m,m})e^{(-\delta_e * \phi_{m,m})} \quad (2)$$

These geometrical parameters were then used in the Costa et al. (2009) model to define the apparent viscosity of the frictional melt suspensions; here, considering the mass movements' runout speeds of >10 m s^{-1} (Legros, 2002 and references therein) and the preserved frictional melt thickness of 12 mm, we estimated the maximum frictional melt strain rate at 10^3 s^{-1} for use in our calculations (Fig. 12b; Table 1). [Whilst we posit that melt generation and thus melt thickness varied temporally and spatially, we used the preserved frictional melt layer thickness to define strain rate here to illustrate the impact of particles on suspension viscosity.] We observe that the presence of solid particles in the frictional melt significantly increase the range of probable viscosities which impact slip during the debris avalanche. Yet, further constraints of suspension viscosity are difficult without knowledge of temperature conditions in the melt.

Frictional melting has commonly been described to be a disequilibrium process occurring via selective melting of mineral phases (Spray, 1992, 2010; Shimamoto and Lin, 1994; Lin and Shimamoto, 1998; Wallace et al., 2019). This provides a framework to evaluate frictional melt temperature based on mineral breakdown temperature. Considering that the frictional melting likely involved both wall rocks and that the pyroxenes, some plagioclase and few amphiboles survived implies that most of the amphiboles, any biotite inherited from the ignimbrite, the interstitial glass and some of the plagioclase likely underwent melting. This analysis suggests that the frictional melt may have reached temperatures of approximately 1200–1300 °C. At such temperatures, the viscosity of the frictional melt preserved in the basal layer would have been $10^{5.1}$ -$10^{4.3}$ Pa s (for the highest silica melt chemistry) and the apparent viscosity of the suspensions at a strain rate of 10^3 s^{-1} (η_{app}) approximately $10^{5.8}$–$10^{5.1}$ Pa s (assuming a nominal 0.1 wt% water dissolved in the melt).

The theory of heat conduction detailed by Carslaw and Jaeger (1959) can be used to estimate slip conditions required to generate temperature change (ΔT):

$$\Delta T = \frac{\mu \sigma_n V \sqrt{t}}{\rho C_p \sqrt{\pi k}} \quad (3)$$

Considering a friction coefficient (μ) of 0.85 (at static conditions; Byerlee, 1978), a normal stress (σ_n) of 2.6 MPa [based on an overburden of 100 m and a bulk rock density (ρ) of 2656.6 kg m^{-3} (as determined by

He-pycnometry)], a specific heat capacity (C_p) of 900 J kg^{-1} K^{-1}, and a thermal diffusivity (k) of 10^{-6} m^2 s^{-1}, we can bracket slip velocity (V) and duration (t) along the basal contact. Given that distance (d) is proportional to the products of slip rate and duration, $d = Vt$, the above analysis suggests that frictional melting (reaching a nominal temperature of 1250 °C), would have occurred in <2 m if the slip velocity was greater than 5 m s^{-1}. Fig. 12c shows that for more rapid slip rates, the distance of slip required for melting would have been shorter. This does not agree with the observation that only a thin pseudotachylyte was observed at much greater runout distances of 24 km. Yet, considering that the basal contact did not generate (or preserve) a pseudotachylyte at a slip distance of 17.5 km, it suggests that the slip conditions must have locally evolved rapidly during the avalanche, highlighting the transient nature of slip during debris avalanches, including the potential reduction of μ during dynamic slip. Thus, we must turn to other proxies to define local slip rate conditions that led to frictional melting.

The early occurrence of frictional melt fragmentation, as witnessed by the presence of pseudotachylyte fragments (with different chemistry to the main pseudotachylyte) in the marginal cataclastic region of the shear zone, demands further appraisal. Silicate melts are viscoelastic bodies which abide by Maxwell's structural relaxation concept (Dingwell and Webb, 1989), where the timescale of relaxation (τ) is proportional to the ratio between the melt's shear viscosity (η) and the elastic modulus at infinite frequency (G_∞, approximated at 10^{10} Pa for silicate melts at relevant conditions; Webb and Dingwell, 1990):

$$\tau = \frac{\eta}{G_\infty} \tag{4}$$

In rheological analysis, if the timescale of observation (t_{obs}) approaches the relaxation timescale, the material exhibits increasingly elastic behaviour and may rupture if the accumulated stress is sufficient. This can be accessed via the dimensionless Deborah number (De), whereby $De_0 = \frac{\tau}{t_{obs}}$. It has been found that silicate melts tend to rupture at strain rates two orders of magnitude lower than that predicted by viscoelasticity theory; that is, at a critical Deborah limit, $De_{c,0} = 10^{-2}$ (Webb and Dingwell, 1990). Thus, the critical timescale for rupture has commonly been simplified to $\tau_c = \frac{\eta}{De_{c,0} G_\infty}$ (Lavallée et al., 2015). Given that the inverse of the relaxation timescale corresponds to the structural relaxation timescale $\dot{\varepsilon} = 1/\tau$, Lavallée et al. (2015) coined the following expression to define the strain rate at which a frictional melt would undergo rupture ($\dot{\varepsilon}_{max}$):

$$\dot{\varepsilon}_{max} = \frac{De_{c,0} G_\infty}{\eta} \tag{5}$$

Assuming that shear is distributed across the entire thickness of the frictional melt layer ($z \cong 12$ mm), they suggest that we can estimate the maximum slip rate (V_{max}) using

$$V_{max} = \frac{De_{c,0} G_\infty z}{\eta} \tag{6}$$

Considering an early frictional melt viscosity (η_e) estimate of $10^{4.4}$ Pa s, Eq. (5) would suggest that the melt phase underwent a strain rate greater than $10^{3.6}$ s^{-1} and Eq. (6) would constrain the local slip velocity at 46.9 m s^{-1}. However, the presence of the solid fragments and bubbles in the melt layer would have also modified the rheological conditions leading to rupture (e.g. Coats et al., 2018); thus any modelling of frictional melt rheology should account for the complexity borne by suspended particles. Here we detail how to implement this analysis. Cordonnier et al. (2012) suggested that the fraction of crystals in suspension (ϕ_x) would lower the critical Deborah number ($De_{c,x}$) following:

$$De_{c,x} = De_{c,0}\left(1 - \frac{\phi_x}{\phi_{m,e}}\right) \tag{7}$$

where $\phi_{m,e}$ is the maximum packing value estimated for the frictional melt at 0.73 for the early fragmented pseudotachylyte and 0.71 for the later preserved layer. The fraction of bubbles (ϕ_b) in the suspension would have similarly lowered the critical Deborah limit of the suspension ($De_{c,s}$), which according to Coats et al. (2018) would follow:

$$De_{c,s} = 1.7 \times 10^{-4}\phi_b + De_{c,x} \tag{8}$$

which can be rewritten as

$$De_{c,s} = 1.7 \times 10^{-4}\phi_b + De_{c,0}\left(1 - \frac{\phi_x}{\phi_{m,e}}\right) \tag{9}$$

So, considering this failure criterion in our previous analysis of maximum strain rate and slip velocity experienced by the frictional melt, we can rewrite Eqs. (5) and (6), by considering $De_{c,s}$ instead of $De_{c,0}$, obtaining:

$$\dot{\varepsilon}_{max} = \left(1.7 \times 10^{-4}\phi_b + 10^{-2}\left(1 - \frac{\phi_x}{\phi_{m,e}}\right)\right)\frac{G_\infty}{\eta} \tag{10}$$

And

$$V_{max} = \left(1.7 \times 10^{-4}\phi_b + 10^{-2}\left(1 - \frac{\phi_x}{\phi_{m,e}}\right)\right)\frac{G_\infty z}{\eta} \tag{11}$$

respectively. As the fragmented pseudotachylyte has interstitial melt with a viscosity of $10^{4.4}$ Pa s and contains $\phi_x = 0.25$ and $\phi_b = 0.14$, we estimate rupture occurred when the strain rate exceeded ~$10^{3.4}$ s^{-1} which would have occurred when the slip velocity exceeded at least 31 m s^{-1} during debris avalanche (Fig. 12d); this critical slip velocity (for fragmentation) may have been higher for less evolved schlieren present in this early frictional melt. The same calculation for the later formed preserved layer using interstitial melt viscosity (η_l) of $10^{4.7}$ Pa s, $\phi_x = 0.43$, $\phi_b = 0.15$ and $\phi_{m,l} = 0.71$ gives a lower maximum velocity of 9.6 m s^{-1} for the most evolved schlieren within the late frictional melt (but higher values for the less evolved melt filaments). So, these rheological constraints provide a view that the slip velocity varied during the debris avalanche.

Finally, in order to assess the rheological impact of frictional melt on debris avalanches, we compare the shear resistance (σ_s) of the modelled melt layers to the shear resistance that would occur in a purely frictional, rock-rock slip environment (i.e., without melt). To do this, we use the viscosity equation:

$$\sigma_s = \eta_{app}\dot{\varepsilon} \tag{12}$$

where the strain rate for the layer modelled is calculated by:

$$\dot{\varepsilon} = \frac{V}{z} \tag{13}$$

Frictional melt suspension viscosity (η_{app}) previously calculated (see Table 1) following Costa et al. (2009) constrains the range of shear resistance imposed by the frictional melt onto slip at 4.7–56.1 MPa, evolving to 22.1–260.4 MPa with further slip (under the same conditions). In contrast, the frictional resistance of rock-rock slip at the base of the deposit may be estimated using Byerlee's frictional law of $\sigma_s = \mu\sigma_n$ (Byerlee, 1978); assuming a friction coefficient of 0.85 and a normal stress, $\sigma_n = \rho g D = 2.6$ MPa, we estimate the shear resistance during rock-rock sliding at 2.2 MPa. Comparing the shear resistances offered by rock-rock friction versus frictional melt, we find that the shear resistance calculated for the melt layer at 10^3 s^{-1} strain rate exceeds that predicted by Byerlee's frictional law. Yet, we surmise that the rate weakening tendency of rock-rock friction (Fialko and Khazan, 2005) would likely promote even lower shear resistances at the slip rates of meters/seconds described in this section. However, local variations in chemistry, solid fraction and temperature would have promoted strain localisation which may have drastically impacted the resultant shear resistance during slip. It must be noted here, that the modelled apparent viscosities of the frictional melts may have been overestimated as they are

constrained at a strain rate (10^3 s^{-1}) exceeding the empirically validated strain rate limit (10^{-1} s^{-1}) of the Costa et al. (2009) model. Beyond that limit, the model assumes (hence predicts) that the apparent viscosity no longer decreases as a function of strain rate (i.e., that slip with frictional melt no longer undergoes rate weakening at such extreme rates); thus the shear resistance (calculated for a given viscosity) increases with strain rate, though this remains untested. Further rheological experiments at such extreme rates are required to improve our ability to model the rapid shear regime extant in sector collapse events.

6. Discussion

6.1. Emplacement style

The palaeotopography of the original land surface included ridges and gullies as evidenced by the preserved palaeotopography and lahar deposits which are restricted to narrow channels in the ignimbrite. Clastic dyking may have resulted from the avalanche crossing fluid rich areas of palaeotopography such as riverbeds, or simply saturated regions of the porous ignimbrite. Local flow directions at Loc. 1 (Fig. 2) indicate that the debris avalanche was at least partially directed by local topography, which may be especially relevant near the thinned margins.

In each locality investigated there appears to be very little range in lithic composition. Although little literature exists on the composition of eruptive and intrusive products from Pichu Pichu, the observations made here suggest that the volcanic edifice-forming rocks are consistent with intermediate volcanic products typical of a compound volcano present in the Andes. The homogeneity of the surviving clasts within the flow in the areas studied therefore suggests there was limited internal shear that would have enhanced mixing of different lithologies during the debris avalanche. This is supported by the sharp contact between compositionally different flow packages at Loc. 1 (see Fig. 2e–f). Such separation of flow packages suggests that overall, the flow mostly moved as discrete bodies, though without knowledge of the volcanic units incorporated this interpretation is speculative. Higher up in the flow at Loc. 3 away from high shear at the basal contact, large clasts have been transported intact. In this survey, as the studied shear structures were all in distal localities, it is difficult to convey any constraint about coherence within the core of the flow. Several field mapping studies of collapse deposits have previously noted that mixed-matrix supported facies are rare in deposit cores, but were more common in marginal regions (Glicken, 1998; Belousov et al., 1999). These studies have highlighted that the centre of deposits and proximal areas consist of larger blocks in block-supported facies.

6.2. Evolving degree of strain localisation

The basal sliding surface or shear zone of a mass movement is subjected to extreme shear conditions (Erismann and Abele, 2001). As noted at Loc. 1 there is evidence for intense shearing in the lower 2–3 m of the flow, causing the destruction of large clasts, forming a matrix-dominated, well-sorted granular layer. The presence of a matrix-supported basal layer has previously been observed at other avalanche deposits worldwide, such as at Parinacota (Chile) where structureless sedimentary layers occur at the base of each deposit and are interpreted to originate from the localisation of shear during emplacement (Clavero et al., 2002). Similarly, the small grain sizes in the lower 1 m at the base of multiple debris avalanche deposits from Shiveluch (Kamchatka peninsula, Russia), has also been interpreted as the result of shear localisation at the base of a debris flow (Belousov et al., 1999). Although none are associated with a basal pseudotachylyte, it is an indicator of the common occurrence of basal shear localisation and comminution in volcanic debris avalanches. The extreme localisation to produce frictional melting, as seen at Loc. 1 in this study, is still rarely reported. However, earlier studies on this phenomenon at field sites such as Langtang (Nepal: Masch et al., 1985) and Kofels (Austria; Erismann, 1979) have been joined by more recent studies on Markagunt gravity slide in Utah (Hacker et al., 2014), Heart Mountain in Wyoming (Goren et al., 2010), Mont Dore volcanic massif (France; Bernard and van Wyk de Vries, 2017) and a rockslide near Kanchenjunga (Nepal; Weidinger and Korup, 2009) where further landslide generated pseudotachylytes have been identified.

Observations made in Loc. 2 suggest that basal granular zones may be subjected to a high degree of strain localisation, as observed by an area of pervasive cataclastic shear crosscut by a fault surface, showing slip transfer upon enhanced localisation. Such cross-cutting behaviour, indicative of an increased degree of strain localisation, was further observed in the intra-body shear zones, suggesting that these switches in the degree of strain localisation may not necessarily be restricted to the basal shear zone, but may affect the development of the avalanche as a whole. This may be likely if shear occurs in an unfavourable region as in cases where a contact is uneven with asperities (see Loc. 2) or if local topography slopes against the deposit flow direction or during acceleration or deceleration phases. Rough surface topology across all scales would locally induce higher normal stresses which would respectively promote higher shear stresses (and intergranular forces) in this region of the flow, as illustrated by a sketch diagram in Fig. 13. This concentration of stress at the asperities may have promoted the rupture in the granular medium of a new, smoother surface and facilitate flow with lower frictional resistance. This would either act to shift shear to above the asperity (Fig. 13c) and/or remove some or all of the basal asperity (Fig. 13d), incorporating the fragmented materials in the flow, and promoting shear on a smooth surface as seen at Loc. 2 (Fig. 3e–f). Evidence for both mechanisms are seen, first by the generation of secondary slip surfaces and second by incorporation of ignimbrite material into the flow deposit. The Koefels landslide in Austria underwent a similar process but at a larger scale, forming new internal slip surfaces upon encountering a topographic barrier (in this case a valley wall) (Erismann, 1979). This is somewhat similar to the decoupling process in pyroclastic density currents and block-and-ash flows, where the dilute upper portion of the flow can detach from the lower flow and override a topographic barrier and even travel in a different direction to the lower flow (Fisher, 1995; Douillet et al., 2013). Here, the outcrops at Loc. 1 show 2 distinct zones of shear localisation at different levels within the flow body, similar to the suggestion of De Blasio and Elverhøi (2008).

6.3. Frictional melting

As pseudotachylytes were not ubiquitous along the basal contact, we advance that the generation of frictional melt at the base of debris avalanches may be considered to be both spatially and temporally discontinuous. The occurrence of a fluidised basal layer with enhanced injection and mixing, seen at Loc. 3 and in other landslides (Anders et al., 2010; Craddock et al., 2012) can prevent the strain localisation necessary for frictional melting. Melt formation in volcanic collapses is highly dependent on the conditions (including normal stress from overburden and pore pressure) (Legros, 2002; Nielsen et al., 2008; Violay et al., 2014), extent and rate of shear localisation (Magloughlin and Spray, 1992; De Blasio and Elverhøi, 2008), heat generation versus diffusion away from slip surface (Carslaw and Jaeger, 1959), any residual heat from volcanism, surface topography and roughness (Nielsen et al., 2010), and the melting points and shear strength of the materials (Spray, 1992), many of which would vary and evolve during transport. This may in part explain the common absence of pseudotachylyte at the basal contacts of debris avalanche deposits worldwide, which may also be a result of alteration or destruction (Kirkpatrick and Rowe, 2013). As modelled in section 5.4, debris avalanches flowing at high rates (along one or several thin shear zones) may promote shear rates likely to exceed the structural relaxation of frictional melts to induce brittle failure, preventing preservation.

The maximum strain rates that may be accommodated by the thickness of the inhomogeneous melt layer observed indicates that the

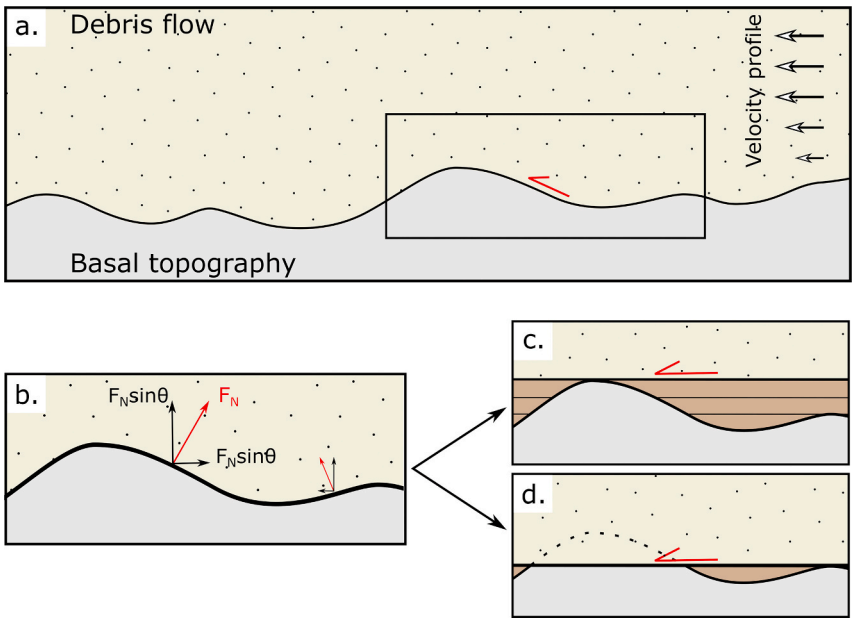

Fig. 13. Sketch diagrams illustrating successive shear localisation by rupture or asperity ploughing (may occur at a range of scales). a) A rough surface with velocity profile (indicated by arrow size). b) A rough surface influencing normal, compressive force (F_N) induced by topography. c) Scenario 1, faster moving upper flow propagates along a newly formed shear surface. d) Scenario 2, an asperity is removed by fracturing and is incorporated into the flow.

flow exceeded ~31 m s^{-1} to fragment it. However, the higher modelled viscosity of the preserved layer suggests that it would have fragmented at slip velocities exceeding 9.6 m s^{-1} (at the estimated temperatures). As the layer has remained intact, this suggests that the flow slowed between the fragmentation of the early melt-bearing layer and the formation of the preserved melt-bearing layer. This may also imply that the shear was localised elsewhere, a hypothesis supported by the occurrence of a secondary slip surface above the basal contact at this locality, or the layer preserved in the outcrop was a late stage feature formed as the flow slowed. Thus, slip velocity may dynamically vary during transport, as a function of distance, palaeotopography and strain partitioning onto different fault surfaces; such contrasting slip conditions may promote compressional and extensional regimes in the flow, which could induce secondary shear zones and intrusion of clastic dykes.

Although frictional melts are commonly regarded as potential lubricating layers promoting increased runout distances (Erismann, 1979; De Blasio and Elverhøi, 2008), the rheological comparison of the apparent viscosity to Byerlee (1978) friction indicates that frictional melting is unlikely to have lessened the basal shear resistance at the high shear rates expected; even though the early frictional melt (prior to fragmentation) exhibited a relatively low apparent viscosity. Additionally, variation in melt layer thickness, temperature, and the incorporation of both exsolved and dissolved water from the breakdown of amphiboles could have rheologically impacted the development of frictional melts and promoted lubrication through time. If the formation of pseudotachylyte is a cyclic process in which melting may be followed by fragmentation (if strain rate is too high) and slip re-localisation onto a new fault plane, then the lubricating or viscous braking effects of frictional melts may equally be cyclic. It must be noted that variability in chemistry and, importantly, crystallinity during selective melting and melt homogenisation controls the rheological evolution of frictional melt (Spray, 2010; Wallace et al., 2019) and whether lubrication or viscous brake locally develops with slip.

7. Concluding remarks

The Arequipa volcanic landslide deposit originated from the sector collapse of Pichu Pichu volcano and forms an area of elevated hummocky topography approximately 300 m thick at its maxima, which extends 26 km west from the dissected volcanic complex in a broad, fan-like shape that covers ~200 km^2. The andesitic debris avalanche, which likely exceeded 20 km^3 in volume, ramped up over a palaeotopography of ignimbrite during runout.

The subsequent deposition of eruption products of other proximal volcanoes and the incision of rivers into the deposit obscures the original topography. However, river valleys reveal the basal contact and structures within the lower portion of the flow. Field examination, chemical analyses and microstructural observations highlight the complex nature of shear during the debris avalanche. We observed evidence of a variety of shear deformation mechanisms (cataclasis and frictional melting), degrees of strain localisation, and strain partitioning across the body of the flow (summarised in Fig. 14).

The basal contacts show varying degrees of shear localisation. The first example evidences a high level of shear with near total fragmentation of clasts near the basal contact and extreme localisation of shear to form a thin layer of pseudotachylyte. Fragments of pseudotachylyte within the cataclasite at the base suggests multiple generations of melt. Geochemical results combined with rheology modelling are used to suggest that the fragmentation of melt layers could be attributed to high strain rates that forced the melt into brittle rupture, thus limiting the chance of a persisting melt layer. Contrastingly, the second locality studied has a more diffuse basal shear zone, less fragmentation of clasts, multiple fracture sets and crosscutting slip surfaces that show slip zone evolution and indicate more distributed shear.

Within the lower portion of the debris avalanche body, at several localities, secondary shear zones are observed in the deposit. This highlights the propensity to delocalise shear from the basal plane to be accommodated on other discrete planes. Additionally, we note the presence of clastic dyking which likely originates from the basal plane and suggests the presence of a pressurised, fluidised layer in some areas that may have been enhanced by crossing of river beds or water saturation of the underlying porous ignimbrite. The interaction of clastic dykes, shear planes and the juxtaposition of distinct flow units suggests that active shearing planes acted as barrier layers limiting material mixing and causing segregation of the flow.

We conclude that shear localisation can occur at both the basal contact and on discrete planes within the flow and that frictional melting at the debris flow base may be possible at areas of extreme localisation of

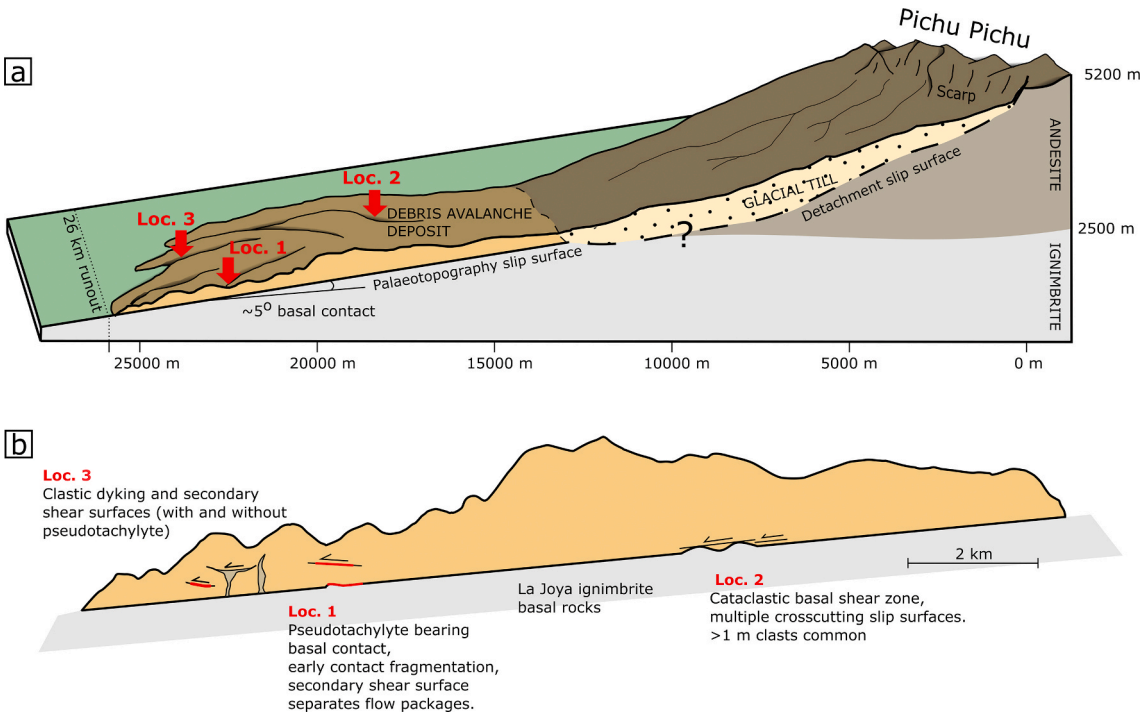

Fig. 14. Sketches outlining preserved processes in the Pichu Pichu debris avalanche deposit. a) Scaled sketch illustrating deposit, source and studied outcrops in this study. b) Flattened idealised cross section of features of the flow interior (topography scale increased by factor of 2 and features not to scale) summarising the observations of the field study and variation in basal shear zone morphology.

shear. However, it is unlikely that frictional melt aided lubrication at the base or that it persisted throughout the debris avalanche deposition, instead local deformation mechanisms at the flow base likely switched rapidly. The localisation of shear can therefore change both through time and spatially across the flow due to topographic, lithological and environmental changes of the land surface.

CRediT authorship contribution statement

Amy Hughes: Conceptualization, Methodology, Formal analysis, Investigation, Writing - original draft, Writing - review & editing, Visualization, Project administration, Funding acquisition. **Jackie E. Kendrick:** Conceptualization, Methodology, Formal analysis, Investigation, Writing - original draft, Writing - review & editing, Visualization, Supervision, Project administration, Funding acquisition. **Guido Salas:** Investigation, Writing - original draft, Writing - review & editing. **Paul A. Wallace:** Methodology, Writing - original draft, Writing - review & editing, Visualization. **François Legros:** Investigation, Writing - original draft, Writing - review & editing. **Giulio Di Toro:** Methodology, Writing - original draft, Writing - review & editing, Visualization, Supervision. **Yan Lavallée:** Conceptualization, Methodology, Formal analysis, Investigation, Resources, Writing - original draft, Writing - review & editing, Visualization, Supervision, Project administration, Funding acquisition.

Declaration of competing interest

The authors declare that they have no known competing financial interests or personal relationships that could have appeared to influence the work reported in this paper.

Acknowledgements

This work was conducted during a PhD study supported by the Natural Environment Research Council (NERC) EAO Doctoral Training Partnership and is fully funded by NERC whose support is gratefully acknowledged (Grant Number NE/L002469/1). We acknowledge financial support from the European Research Council Starting Grant on Strain Localisation in Magma (SLiM, No. 306488) and Jackie Kendrick was supported by an Early Career Fellowship of the Leverhulme Trust (ECF-2016-325). We also thank Tom Knott (University of Leicester) for XRF measurements and Jonathan Fellowes (University of Manchester) for technical assistance during EPMA analysis. We thank the editor Joao Hippertt and an anonymous reviewer for their well-thought, precise and constructive comments.

Appendix A. Supplementary data

Supplementary data to this article can be found online at https://doi.org/10.1016/j.jsg.2020.104132.

References

Acocella, V., Puglisi, G., 2010. Hazard mitigation of unstable volcanic edifices. EOS Trans 91. https://doi.org/10.1029/2010EO400002.

Aguilar Contreras, R., Thouret, J.-C., Samaniego Eguiguren, P., 2016. Actividad eruptiva en sistemas de larga duración: relaciones entre el complejo post-caldérico Chachani y las ignimbritas Plio-cuaternarias de la cuenca de Arequipa (Perú). Congreso Peruano de Geología, Lima, PE, 16-19 Octubre 2016, Resúmenes 18.

Anders, M., Fouke, B., Zerkle, A., Tavarnelli, E., Alvarez, W., Harlow, G., 2010. The role of calcining and basal fluidization in the long runout of carbonate slides: an example from the Heart mountain slide block, Wyoming and Montana. U.S.A. J Geol 118. https://doi.org/10.1086/656383.

Arabnia, O., Sklar, L., 2016. Experimental study of particle size reduction in geophysical granular flows. Int J Erosion Control Eng 9, 122–129. https://doi.org/10.13101/ijece.9.122.

Belousov, A., Belousova, M., Voight, B., 1999. Multiple edifice failures, debris avalanches and associated eruptions in the Holocene history of Shiveluch volcano, Kamchatka, Russia. Bull. Volcanol. 61, 324–342. https://doi.org/10.1007/s004450050300.

Benson, P., Heap, M.J., Lavallée, Y., Flaws, A., Hess, K.-U., Selvadurai, P., Dingwell, D., Schillinger, B., 2012. Laboratory simulations of tensile fracture development in a volcanic conduit via cyclic magma pressurisation. Earth and Planetary Sci Lett 349 (350), 231–239. https://doi.org/10.1016/j.epsl.2012.07.003.

Bernard, K., van Wyk de Vries, B., 2017. Volcanic avalanche fault zone with pseudotachylite and gouge in French Massif Central. J. Volcanol. Geoth. Res. 347, 112–135. https://doi.org/10.1016/J.JVOLGEORES.2017.09.006.

Biek, R.F., Rowley, P.D., Hacker, D.B., 2019. The gigantic Markagunt and sevier gravity slides resulting from mid-cenozoic catastrophic mega-scale failure of the marysvale volcanic field. Utah, USA. https://doi.org/10.1130/FLD056.
Brodsky, E.E., Kanamori, H., 2001. Elastohydrodynamic lubrication of faults. J. Geophys. Res.: Solid Earth 106, 16357–16374. https://doi.org/10.1029/2001JB000430.
Byerlee, J., 1978. Friction of rocks. Pure Appl. Geophys. 116, 615–626. https://doi.org/10.1007/bf00876528.
Calder, E.S., Luckett, R., Sparks, R.S.J., Voight, B., 2002. Mechanisms of lava dome instability and generation of rockfalls and pyroclastic flows at Soufrière Hills Volcano, Montserrat. Geol Soc, London, Memoirs 21, 173–190. https://doi.org/10.1144/GSL.MEM.2002.021.01.08.
Campbell, C.S., Cleary, P.W., Hopkins, M., 1995. Large-scale landslide simulations: global deformation, velocities and basal friction. J. Geophys. Res.: Solid Earth 100, 8267–8283. https://doi.org/10.1029/94JB00937.
Caricchi, L., Burlini, L., Ulmer, P., Gerya, T., Vassalli, M., Papale, P., 2007. Non-Newtonian rheology of crystal-bearing magmas and implications for magma ascent dynamics. Earth Planet Sci. Lett. 264, 402–419. https://doi.org/10.1016/j.epsl.2007.09.032.
Carslaw, H.S., Jaeger, J.C., 1959. Conduction of Heat in Solids. Clarendon Press, Oxford.
Cecchi, E., van Wyk de Vries, B., Lavest, J.-M., 2004. Flank spreading and collapse of weak-cored volcanoes. Bull. Volcanol. 67, 72–91. https://doi.org/10.1007/s00445-004-0369-3.
Clavero, J., Sparks, R.S.J., Huppert, H., Wb, D., 2002. Geological constraints on the emplacement mechanism of the Parinacota debris avalanche, Northern Chile. Bull. Volcanol. 64, 40–54. https://doi.org/10.1007/s00445-001-0183-0.
Coats, R., Kendrick, J., Wallace, P., Miwa, T., Hornby, A., Ashworth, J., Matsushima, T., Lavallée, Y., 2018. Failure criteria for porous dome rocks and lavas: a study of Mt. Unzen, Japan. Solid Earth 9, 1299–1328. https://doi.org/10.5194/se-9-1299-2018.
Cordonnier, B., Caricchi, L., Pistone, M., Castro, J., Hess, K.-U., Gottschaller, S., Manga, M., Dingwell, D.B., Burlini, L., 2012. The viscous-brittle transition of crystal-bearing silicic melt: direct observation of magma rupture and healing. Geology 40, 611–614. https://doi.org/10.1130/G3914.1.
Costa, A., Caricchi, L., Bagdassarov, N., 2009. A model for the rheology of particle-bearing suspensions and partially molten rocks. G-cubed 10. https://doi.org/10.1029/2008GC002138.
Craddock, J.P., Geary, J., Malone, D.H., 2012. Vertical injectites of detachment carbonate ultracataclasite at White Mountain, Heart Mountain detachment, Wyoming. Geology 40, 463–466. https://doi.org/10.1130/G32734.1.
Davies, T.R., McSaveney, M.J., 2009. The role of rock fragmentation in the motion of large landslides. Eng. Geol. 109, 67–79. https://doi.org/10.1016/j.enggeo.2008.11.004C.
Davies, T.R.H., 1982. Spreading of rock avalanche debris by mechanical fluidization. Rock Mech. 15, 9–24. https://doi.org/10.1007/BF01239474.
Day, S.J., 1996. Hydrothermal pore fluid pressure and the stability of porous, permeable volcanoes. Geol Soc, London, Special Publ 110, 77–93. https://doi.org/10.1144/gsl.sp.1996.110.01.06.
De Blasio, F.V., 2011. Landslides in Valles Marineris (Mars): a possible role of basal lubrication by sub-surface ice. Planet. Space Sci. 59, 1384–1392. https://doi.org/10.1016/J.PSS.2011.04.015.
De Blasio, F.V., Elverhøi, A., 2008. A model for frictional melt production beneath large rock avalanches. J. Geophys. Res.: Earth Surface 113. https://doi.org/10.1029/2007JF000867 n/a.
de Silva, S.L., Francis, P.W., 1990. Potentially active volcanoes of Peru-observations using landsat thematic mapper and space shuttle imagery. Bull. Volcanol. 52, 286–301. https://doi.org/10.1007/BF00304100.
Di Toro, G., Hirose, T., Nielsen, S., Pennacchioni, G., Shimamoto, T., 2006. Natural and experimental evidence of melt lubrication of faults during earthquakes. Science 311, 647–649. https://doi.org/10.1126/science.1121012.
Dingwell, D.B., Webb, S.L., 1989. Structural relaxation in silicate melts and non-Newtonian melt rheology in geologic processes. Phys. Chem. Miner. 16, 508–516. https://doi.org/10.1007/bf00197020.
Douillet, G.A., Tsang-Hin-Sun, È., Kueppers, U., Letort, J., Pacheco, D.A., Goldstein, F., Von Aulock, F., Lavallée, Y., Hanson, J.B., Bustillos, J., Robin, C., Ramón, P., Hall, M., Dingwell, D.B., 2013. Sedimentology and geomorphology of the deposits from the August 2006 pyroclastic density currents at Tungurahua volcano, Ecuador. Bull. Volcanol. 75, 765. https://doi.org/10.1007/s00445-013-0765-7.
Erismann, T., Abele, G., 2001. Dynamics of rockslides and rockfalls. https://doi.org/10.1007/978-3-662-04639-5.
Erismann, T.H., 1979. Mechanisms of large landslides. Rock Mech. 12, 15–46. https://doi.org/10.1007/bf01241087.
Ferri, F., Di Toro, G., Hirose, T., Han, R., Noda, H., Shimamoto, T., Quaresimin, M., de Rossi, N., 2011. Low- to high-velocity frictional properties of the clay-rich gouges from the slipping zone of the 1963 Vaiont slide, northern Italy. J. Geophys. Res.: Solid Earth 116. https://doi.org/10.1029/2011JB008338.
Fialko, Y., Khazan, Y., 2005. Fusion by earthquake fault friction: stick or slip? J. Geophys. Res. 110 https://doi.org/10.1029/2005JB003869.
Fisher, R.V., 1995. Decoupling of pyroclastic currents: hazards assessments. J. Volcanol. Geoth. Res. 66, 257–263. https://doi.org/10.1016/0377-0273(94)00075-R.
Giordano, D., Russell, J.K., Dingwell, D.B., 2008. Viscosity of magmatic liquids: a model. Earth Planet Sci. Lett. 271, 123–134. https://doi.org/10.1016/J.EPSL.2008.03.038.
Glicken, H., 1998. Rockslide-debris avalanche of may 18, 1980, Mount St. Helens volcano, Washington. Bull. Geol. Surv. Jpn. 49, 96–677.
Glicken, H., 1991. Sedimentary architecture of large volcanic-debris avalanches. Sedimentation in Volcanic Settings 45, 99–106. https://doi.org/10.2110/pec.91.45.0099.
Goren, L., Aharonov, E., Anders, M.H., 2010. The long runout of the Heart Mountain landslide: heating, pressurization, and carbonate decomposition. J. Geophys. Res.: Solid Earth 115. https://doi.org/10.1029/2009JB007113.
Hacker, D.B., Biek, R.F., Rowley, P.D., 2014. Catastrophic emplacement of the gigantic Markagunt gravity slide, southwest Utah (USA): implications for hazards associated with sector collapse of volcanic fields. Geology 42, 943–946. https://doi.org/10.1130/G35896.1.
Heap, M.J., Faulkner, D.R., Meredith, P.G., Vinciguerra, S., 2010. Elastic moduli evolution and accompanying stress changes with increasing crack damage: implications for stress changes around fault zones and volcanoes during deformation. Geophys. J. Int. 183, 225–236. https://doi.org/10.1111/j.1365-246X.2010.04726.x.
Hornby, A.J., Kendrick, J.E., Lamb, O.D., Hirose, T., De Angelis, S., von Aulock, F.W., Umakoshi, K.-U., Miwa, T., Henton De Angelis, S., Wadsworth, F.B., Hess, K., Dingwell, D.B., Lavallée, Y., 2015. Spine growth and seismogenic faulting at Mt. Unzen, Japan. J. Geophys. Res. Solid Earth (120), 4034–4054. https://doi.org/10.1002/2014JB011660.
Hunt, J.E., Cassidy, M., Talling, P.J., 2018. Multi-stage volcanic island flank collapses with coeval explosive caldera-forming eruptions. Sci. Rep. 8, 1146. https://doi.org/10.1038/s41598-018-19285-2.
Iverson, R.M., George, D.L., Allstadt, K., Reid, M.E., Collins, B.D., Vallance, J.W., Schilling, S.P., Godt, J.W., Cannon, C.M., Magirl, C.S., Baum, R.L., Coe, J.A., Schulz, W.H., Bower, J.B., 2015. Landslide mobility and hazards: implications of the 2014 Oso disaster. Earth Planet Sci. Lett. 412, 197–208. https://doi.org/10.1016/J.EPSL.2014.12.020.
Johnson, B.C., Campbell, C.S., Melosh, H.J., 2016. The reduction of friction in long runout landslides as an emergent phenomenon. J. Geophys. Res.: Earth Surface 121, 881–889. https://doi.org/10.1002/2015JF003751.
Kaneoka, I., Guevara, C., 1984. K-Ar determinations of late Tertiary and Quaternary Andean volcanic rocks, Southern Peru. Geochem. J. 18, 233–239. https://doi.org/10.2343/geochemj.18.233.
Kawamura, S., Miura, S., 2013. Rainfall-induced failures of volcanic slopes subjected to freezing and thawing. Soils Found. 53, 443–461. https://doi.org/10.1016/J.SANDF.2013.04.006.
Kendrick, J.E., Lavallée, Y., Ferk, A., Perugini, D., Leonhardt, R., Dingwell, D.B., 2012. Extreme frictional processes in the volcanic conduit of Mount St. Helens (USA) during the 2004–2008 eruption. J. Struct. Geol. 38, 61–76. https://doi.org/10.1016/j.jsg.2011.10.003.
Kendrick, J.E., Lavallée, Y., Hirose, T., Di Toro, G., Hornby, A.J., De Angelis, S., Dingwell, D.B., 2014. Volcanic drumbeat seismicity caused by stick-slip motion and magmatic frictional melting. Nat. Geosci. 7, 438–442. https://doi.org/10.1038/ngeo2146. http://www.nature.com/ngeo/journal/v7/n6/abs/ngeo2146.html#supplementary-information.
Kirkpatrick, J.D., Rowe, C.D., 2013. Disappearing ink: how pseudotachylytes are lost from the rock record. J. Struct. Geol. 52, 183–198. https://doi.org/10.1016/J.JSG.2013.03.003.
Klein, J., Mueller, S.P., Castro, J.M., 2017. The influence of crystal size distributions on the rheology of magmas: new insights from analog experiments. G-cubed 18, 4055–4073. https://doi.org/10.1002/2017GC007114.
Lagmay, A.M.F., van Wyk de Vries, B., Kerle, N., Pyle, D.M., 2000. Volcano instability induced by strike-slip faulting. Bull. Volcanol. 62, 331–346. https://doi.org/10.1007/s004450000103.
Lavallée, Y., de Silva, S.L., Salas, G., Byrnes, J.M., 2009. Structural control on volcanism at the ubinas, huaynaputina, and ticsani volcanic group (UHTVG), southern Peru. J. Volcanol. Geoth. Res. 186, 253–264. https://doi.org/10.1016/J.JVOLGEORES.2009.07.003.
Lavallée, Y., Hess, K.U., Cordonnier, B., Dingwell, D.B., 2007. Non-Newtonian rheological law for highly crystalline dome lavas. Geology 35, 843–846.
Lavallée, Y., Hirose, T., Kendrick, J.E., Hess, K.-U., Dingwell, D.B., 2015. Fault rheology beyond frictional melting. Proc. Natl. Acad. Sci. Unit. States Am. 112.
Lavallée, Y., Mitchell, T.M., Heap, M.J., Vasseur, J., Hess, K.-U., Hirose, T., Dingwell, D. B., 2012. Experimental generation of volcanic pseudotachylytes: constraining rheology. J. Struct. Geol. 38, 222–233. https://doi.org/10.1016/j.jsg.2012.02.001.
Lebti, P.P., Thouret, J.-C., Wörner, G., Fornari, M., 2006. Neogene and quaternary ignimbrites in the area of Arequipa, southern Peru: stratigraphical and petrological correlations. J. Volcanol. Geoth. Res. 154, 251–275. https://doi.org/10.1016/j.jvolgeores.2006.02.014.
Legros, F., 2002. The mobility of long-runout landslides. Eng. Geol. 63, 301–331. https://doi.org/10.1016/S0013-7952(01)00090-4.
Legros, F., Cantagrel, J., Devouard, B., 2000. Pseudotachylyte (frictionite) at the base of the Arequipa volcanic landslide deposit (Peru): implications for emplacement mechanisms. J. Geol. 108, 601–611. https://doi.org/10.1086/314421.
Lin, A., Chen, A., Liau, C.-F., Lee, C.-T., Lin, C.-C., Lin, P.-S., Wen, S.-C., Ouchi, T., 2001. Frictional fusion due to coseismic landsliding during the 1999 Chi-Chi (Taiwan) ML 7.3 Earthquake. Geophys. Res. Lett. 28, 4011–4014. https://doi.org/10.1029/2001GL013253.
Lin, A.M., Shimamoto, T., 1998. Selective melting processes as inferred from experimentally generated pseudotachylytes. J. Asian Earth Sci. 16, 533–545. https://doi.org/10.1016/S0743-9547(98)00040-3.
Lipman, P.W., Mullineaux, D.R., 1981. The 1980 eruptions of Mount St. Helens. Washington, Professional Paper. https://doi.org/10.3133/pp1250.
Lucchitta, B.K., 1987. Valles Marineris, Mars: wet debris flows and ground ice. Icarus 72, 411–429. https://doi.org/10.1016/0019-1035(87)90183-7.
Magloughlin, J.F., 2011. Bubble collapse structure: a microstructural record of fluids, bubble formation and collapse, and mineralization in pseudotachylyte. J. Geol. 119, 351–371. https://doi.org/10.1086/659143.

Magloughlin, J.F., Spray, J.G., 1992. Frictional melting processes and products in geological materials: introduction and discussion. Tectonophysics 204, 197–204. https://doi.org/10.1016/0040-1951(92)90307-R.
Masch, L., Wenk, H.R., Preuss, E., 1985. Electron microscopy study of hyalomylonites—evidence for frictional melting in landslides. Tectonophysics 115, 131–160. https://doi.org/10.1016/0040-1951(85)90103-9.
McGuire, W.J., 1996. Volcano instability: a review of contemporary themes. Geol Soc, London, Special Publ 110, 1–23.
Melosh, H.J., 1986. The physics of very large landslides. Acta Mech. 64, 89–99. https://doi.org/10.1007/BF01180100.
Melosh, H.J., 1979. Acoustic fluidization: a new geologic process? J. Geophys. Res.: Solid Earth 84, 7513–7520. https://doi.org/10.1029/JB084iB13p07513.
Mueller, S., Llewellin, E.W., Mader, H.M., 2010. The rheology of suspensions of solid particles. Proc. Math. Phys. Eng. Sci. 466, 1201–1228. https://doi.org/10.1098/rspa.2009.0445.
Nielsen, S., Di Toro, G., Hirose, T., Shimamoto, T., 2008. Frictional melt and seismic slip. J. Geophys. Res.: Solid Earth 113, B01308. https://doi.org/10.1029/2007jb005122.
Nielsen, S., Mosca, P., Giberti, G., Di Toro, G., Hirose, T., Shimamoto, T., 2010. On the transient behavior of frictional melt during seismic slip. J Geophys Research-Solid Earth 115, 17. https://doi.org/10.1029/2009jb007020.
Phan, S.-E., Russel, W.B., Zhu, J., Chaikin, P.M., 1998. Effects of polydispersity on hard sphere crystals. J. Chem. Phys. 108, 9789–9795. https://doi.org/10.1063/1.476453.
Reid, M.E., 2004. Massive collapse of volcano edifices triggered by hydrothermal pressurization. Geology 32, 373–376. https://doi.org/10.1130/G20300.1.
Scheidegger, A.E., 1973. On the prediction of the reach and velocity of catastrophic landslides. Rock Mech. 5, 231–236. https://doi.org/10.1007/BF01301796.
Schneider, C.A., Rasband, W.S., Eliceiri, K.W., 2012. NIH Image to ImageJ: 25 years of image analysis. Nat. Methods 9, 671–675. https://doi.org/10.1038/nmeth.2089.
Shea, T., van Wyk de Vries, B., 2008. Structural analysis and analogue modeling of the kinematics and dynamics of rockslide avalanchesShea and van Wyk de Vries. Geosphere 4, 657–686. https://doi.org/10.1130/GES00131.1.
Shimamoto, T., Lin, A., 1994. Is frictional melting equilibrium melting or non-equilibrium melting? Struct. Geol. (J. Tect. Res. Gro. Japan) 39, 79–84.
Shreve, R.L., 1968. The blackhawk landslide. In: Shreve, R.L. (Ed.), The Blackhawk Landslide. Geological Society of America. https://doi.org/10.1130/SPE108-p1.
Sibson, R.H., 1977. Fault rocks and fault mechanisms. J. Geol. Soc. 133, 191–213. https://doi.org/10.1144/gsjgs.133.3.0191.
Sibson, R.H., 1975. Generation of pseudotachylyte by ancient seismic faulting. Geophys. J. Roy. Astron. Soc. 43, 775–794. https://doi.org/10.1111/j.1365-246X.1975.tb06195.x.
Siebert, L., 1992. Threats from debris avalanches. Nature 356, 658–659. https://doi.org/10.1038/356658a0.
Siebert, L., 1984. Large volcanic debris avalanches: characteristics of source areas, deposits, and associated eruptions. J. Volcanol. Geoth. Res. 22, 163–197. https://doi.org/10.1016/0377-0273(84)90002-7.
Siebert, L., Glicken, H., Ui, T., 1987. Volcanic hazards from bezymianny- and bandai-type eruptions. Bull. Volcanol. 49, 435–459. https://doi.org/10.1007/BF01046635.
Spray, J., 2010. Frictional melting processes in planetary materials: from hypervelocity impact to earthquakes. Annu. Rev. Earth Planet Sci. 38, 221–254. https://doi.org/10.1146/annurev.earth.031208.100045.
Spray, J.G., 1992. A physical basis for the frictional melting of some rock-forming minerals. Tectonophysics 204, 205–221. https://doi.org/10.1016/0040-1951(92)90308-S.
Swanson, D.A., Duffield, W.A., Fiske, R.S., 1976. Displacement of the south flank of Kilauea Volcano; the result of forceful intrusion of magma into the rift zones. Professional Paper. https://doi.org/10.3133/pp963.
Thouret, J.-C., Finizola, A., Fornari, M., Legeley-Padovani, A., Suni, J., Frechen, M., 2001. Geology of el Misti volcano near the city of Arequipa, Peru. GSA Bull 113, 1593–1610. https://doi.org/10.1130/0016-7606(2001)113<1593:GOEMVN>2.0.CO.
Truby, J.M., Mueller, S.P., Llewellin, E.W., Mader, H.M., 2015. The rheology of three-phase suspensions at low bubble capillary number. Proc. Math. Phys. Eng. Sci. 471, 20140557 https://doi.org/10.1098/rspa.2014.0557.
Violay, M., Di Toro, G., Gibert, B., Nielsen, S., Spagnuolo, E., Del Gaudio, P., Azais, P., Scarlato, P.G., 2014. Effect of glass on the frictional behavior of basalts at seismic slip rates. Geophys. Res. Lett. 41, 348–355. https://doi.org/10.1002/2013GL058601.
Voight, B., 2000. Structural stability of andesite volcanoes and lava domes. Phil. Trans. Roy. Soc. Lond. 358, 1663–1703.
Voight, B., Elsworth, D., 1997. Failure of volcano slopes. Geotechnique 47, 1–31. https://doi.org/10.1680/geot.1997.47.1.1.
Wallace, P.A., De Angelis, S.H., Hornby, A.J., Kendrick, J.E., Clesham, S., von Aulock, F. W., Hughes, A., Utley, J.E.P., Hirose, T., Dingwell, D.B., Lavallée, Y., 2019. Frictional melt homogenisation during fault slip: geochemical, textural and rheological fingerprints. Geochem. Cosmochim. Acta 255, 265–288. https://doi.org/10.1016/J.GCA.2019.04.010.
Wang, Y.F., Dong, J.J., Cheng, Q.G., 2017. Velocity-dependent frictional weakening of large rock avalanche basal facies: implications for rock avalanche hypermobility? J. Geophys. Res.: Solid Earth 122, 1648–1676. https://doi.org/10.1002/2016JB013624.
Webb, S.L., Dingwell, D.B., 1990. The onset of non-Newtonian rheology of silicate melts. Phys. Chem. Miner. 17, 125–132. https://doi.org/10.1007/BF00199663.
Weidinger, J.T., Korup, O., 2009. Frictionite as evidence for a large Late Quaternary rockslide near Kanchenjunga, Sikkim Himalayas, India — implications for extreme events in mountain relief destruction. Geomorphology 103, 57–65. https://doi.org/10.1016/J.GEOMORPH.2007.10.021.